

## Elevated-temperature high-strength *h*-BN-doped Al2014 and Al7075 composites: Experimental and theoretical insights

Shakti Corthay<sup>a</sup>, Konstantin L. Firestein<sup>b</sup>, Dmitry G. Kvashnin<sup>a,c</sup>, Magzhan K. Kutzhanov<sup>a</sup>, Andrei T. Matveev<sup>a</sup>, Andrey M. Kovalskii<sup>a</sup>, Denis V. Leybo<sup>a</sup>, Dmitri V. Golberg<sup>b,d,\*\*</sup>, Dmitry V. Shtansky<sup>a,\*</sup>

<sup>a</sup> National University of Science and Technology "MISIS", Leninsky Prospect 4, Moscow, 119049, Russian Federation

<sup>b</sup> Centre for Materials Science and School of Chemistry and Physics, Faculty of Science, Queensland University of Technology (QUT), 2 George st., Brisbane, QLD, 4000, Australia

<sup>c</sup> Emanuel Institute of Biochemical Physics RAS, 4 Kosigina, Moscow, 119334, Russian Federation

<sup>d</sup> International Centre for Materials Nanoarchitectonics (MANA), National Institute for Materials Scence (NIMS), Namiki 1-1, Tsukuba, Ibaraki, 3050044, Japan



### ARTICLE INFO

#### Keywords:

Metal-matrix composite  
Ball milling  
Spark plasma sintering  
Microstructure  
Tensile strength  
Molecular dynamics simulations

### ABSTRACT

High-strength Al2014 (Al2) and Al7075 (Al7) series composites with and without addition of hexagonal BN (*h*-BN) flakes (1, 3, and 5 wt%) were fabricated from the powder mixtures of individual elements using a combination of high-energy ball milling (HEBM) and spark plasma sintering (SPS). Phase compositions of Al2 and Al7 composites were different from standard alloys obtained via casting and subsequent heat treatment. Thorough structural study revealed the presence of the following phases: Al(Mg,Si,Mn,Fe,Cu), AlCu<sub>x</sub>, MgO<sub>x</sub>, and Al<sub>5</sub>Cu<sub>6</sub>Mg<sub>2</sub> [Al2], Al(Mg,Si,Mn,Fe,Cu), AlCu<sub>x</sub>, Al<sub>5</sub>Cu<sub>6</sub>Mg<sub>2</sub>, Al<sub>6</sub>CuMg<sub>4</sub>, MgO<sub>2</sub>, AlB<sub>2</sub>, and SiN<sub>x</sub> [Al2-BN], Al(Cu,Zn,Mg), Fe(Al, Cu), AlCu<sub>3</sub>, Al<sub>2</sub>Cu/Fe<sub>3</sub>Al, Al<sub>5</sub>Cu<sub>6</sub>Mg<sub>2</sub>, Al<sub>4</sub>Cu<sub>9</sub>, MgO<sub>2</sub> [Al7], and Al(Cu,Zn,Mg), AlCu<sub>x</sub>, MgO<sub>x</sub>, MgN<sub>x</sub>O<sub>y</sub>, MgB<sub>2</sub>, Mg<sub>3</sub>(BO<sub>3</sub>)<sub>2</sub>, BN, and BNO [Al7-BN]. The important role of *h*-BN additives in the microstructure formation during HEBM and SPS was demonstrated. Classical molecular dynamics simulations were carried out to estimate critical shear stress between Al nanoparticles with and without intermediate *h*-BN layers. The obtained results indicated that the *h*-BN nanosheets had provided solid lubrication, prevented nanoparticle agglomeration during HEBM, led to a reduced porosity and more homogeneous reinforcing phase distributions in the powder mixtures and resultant composites. Structural analysis showed, that during SPS, one part of BN additives had reacted with Al, Si, and Mg to form AlB<sub>2</sub>, SiN<sub>x</sub>, and MgB<sub>2</sub>/Mg<sub>3</sub>(BO<sub>3</sub>)<sub>2</sub> inclusions, while the other part remained unreacted and contributed to the material strength. Doping with 3 wt% of BN led to an increase in hardness from 76 HV<sub>10</sub> to 123 HV<sub>10</sub> (Al2 series), and from 97 HV<sub>10</sub> to 130 HV<sub>10</sub> (Al7 series). The maximum room-temperature tensile strength of 310 MPa (Al7-BN) and 235 MPa (Al2-BN) was observed for the samples with 3 wt% of BN, which corresponds to an increase in strength by approximately 74% and 16%, respectively. At elevated temperatures, the tensile strength values were 227 MPa (350 °C) and 221 MPa (500 °C) for Al2-3%BN, and 276 MPa (350 °C) and 187 MPa (500 °C) for Al7-3%BN. The superior mechanical properties were attributed to the combination of high thermal stability of the reinforcing phases, solid solution hardening, and Orowan (precipitation) strengthening.

### 1. Introduction

Light-weight yet high-strength structural materials capable of operating in a wide temperature range are in high demand in aerospace, automobile and sport industries. Compared with other widely used

structural materials (based on Ti, Fe, and Ni) Al is a light-weight metal (densities: Al = 2.7, Ti = 4.5, Fe = 7.8, Ni = 8.94 g/cm<sup>3</sup>) with high thermal conductivity (Al = 237, Ti = 20, Fe = 80, Ni = 90 W/mK) and low electrical resistivity (Al = 0.03, Ti = 0.42, Fe = 0.09, Ni = 0.07 μWm). The disadvantages of Al, in addition to its low melting point (Al

\* Corresponding author.

\*\* Corresponding author. Centre for Materials Science and School of Chemistry and Physics, Science and Engineering Faculty, Queensland University of Technology (QUT), 2 George st., Brisbane, QLD, 4000, Australia.

E-mail addresses: [dmitry.golberg@qut.edu.au](mailto:dmitry.golberg@qut.edu.au) (D.V. Golberg), [shtansky@shs.misis.ru](mailto:shtansky@shs.misis.ru) (D.V. Shtansky).

= 660, Ti = 1670, Fe = 1538, Ni = 1455 °C) and low Young's modulus (Al = 72, Ti = 115, Fe = 215, Ni = 200 GPa) [1], include its low ultimate tensile strength (Al = 30, Ti = 240 MPa) and hardness (Al = 40, Ti = 70 HV) [1], both at room and elevated temperatures.

In this connection, Al, as a structural material, is rarely used in practice in its pure form. At the same time Al is the basis of many alloys and can be strengthened by adding reinforcing nanoparticles. One of the promising additives is boron nitride (BN). This material is chemically inert, non-reactive to most acids, alkalis, and solvents, has high thermal conductivity and stability (up to 900 °C in air and up to 2800 °C in an inert atmosphere) [2]. Among BN polymorphs, hexagonal (graphitic) boron nitride (*h*-BN) is the most stable crystalline form of BN with a layered structure similar to that of graphite (in contrast to which BN is an electrical insulator). Moreover, *h*-BN has a low density (2.29 g/cm<sup>3</sup>), high melting temperature (2973 °C), and good lubricating characteristics both at low and high temperatures.

Even though BN is poorly wetted by metallic (Al, Cu, Zn, Fe, steel, Ge) and non-metallic (Si, B, glass, cryolite, halides) melts [2], the promise of this material as a hardening phase in Al matrix composites has been shown in many works [3–10]. Al/BN composites with high ultimate tensile strength (UTS) were successfully obtained using different powder mixtures and densification methods (Table 1). Maximum strength was achieved using BN microparticles and a combination of high-energy ball milling (HEBM) and spark plasma sintering (SPS). This can be explained by the formation of more homogeneous microstructures in the ball-milled powder mixtures and the resultant SPS composites.

A similar BN reinforcing approach can be applied to Al alloys that have wider practical applications than pure Al. Available data, however, are rather scarce and contradictory while demonstrating either significant improvement or deterioration in mechanical performance with introduction of a reinforcing phase. Table 2 compares the ultimate tensile strength (UTS) values of Al alloys with and without reinforcing additives fabricated by different methods. The highest value of tensile strength of ~425 MPa was reported for Al-2124/Al<sub>2</sub>O<sub>3</sub> composite with 15 wt% of Al<sub>2</sub>O<sub>3</sub> obtained by wet mixing in a vibrating ball mill and cold compacting combined with extrusion [11]. Al-7075 alloy with 1.2 wt% of Al<sub>2</sub>O<sub>3</sub> fabricated by stir-casting also showed a decently high tensile strength [12]. In contrast, some other studies indicated that the UTS value decreased when BN, Al<sub>2</sub>O<sub>3</sub> [11], SiC [13] and graphite [14] had been added. In particular, a drop in tensile strength was explained by decohesion between particles and matrices leading to weak interface bonding [11]. In addition, agglomeration of reinforcing particles and increased porosity had often negatively affected mechanical properties of the composite materials.

In several works, a combination of powder alloy mixing and SPS was used. For example, Al-20Cu-15Mn alloy was fabricated by turbulent mixing and SPS. This demonstrated UTS values of 89 MPa [23]. 2xxx [24] and 7xxx series Al-based alloys were also produced via a

**Table 2**

UTS values of Al alloys with and without reinforcing additives fabricated by different methods.

Composition	Powder mixing technique	Densification technique	UTS [MPa]	Ref.
Al-Cu <sub>4</sub> Mg <sub>1</sub>		Cold compacted,	419	[15]
Al-Cu <sub>4</sub> Mg <sub>1</sub> /5 wt% BN	Wet mixed in vibrating ball mill	extruded	377	
Al 2014		Stir ultrasonic squeeze casting	40	[14]
Al 2014/1 wt% Gr			18	
Al 2014–1 wt% B <sub>4</sub> C			350	
Al-2124	–	Cold compacted,	416	[11]
Al-2124/5 wt% BN	Wet mixed in vibrating ball mill	extruded	377	
Al-2124/15 wt% Al <sub>2</sub> O <sub>3</sub>			425	
Al 7075		Stir casting	220	[16]
Al 7075/9 wt% B <sub>4</sub> C/3 wt% BN			282	
Al 7075/1.5 wt% graphene nano-platelets	Stir casting		155	[17]
Al 7075	Stir casting		120	[12]
Al 7075/1.2 wt% Al <sub>2</sub> O <sub>3</sub>			400	
Al 7075	Stir casting		87	[13]
Al 7075/15 wt% SiC			63	
Al 7075/5 wt% Gr/6 wt% bagasse ash	Stir casting		299	[18]
Al-Zn-Mg-Cu (7075)	–	Cold compacted, extruded	338	[19]
Al 7075	Stir casting		65	[20]
Al 7075-T6/5 wt% SiC/5 wt%h-BN			198	
Al 7075-T6/5 wt% SiC/5 wt%Gr			247	
Al 7075-T6/5 wt% SiC/5 wt%h-MoS <sub>2</sub>			137	
Al 7085	–	Sintering, hot pressed, extruded	277	[21]
Al 7085/15 vol% SiC	Bi-axis rotary mixer		369	
Al 7085/vol% SiC-1 wt.% Mg			357	
Al 7150	Double stir casting		114	[22]
Al 7150/1 wt% SiC	Double stir casting and ultrasonic vibration		120	
Al 7150/1 wt% SiC	Double stir casting, ultrasonic vibration, and vortex stirring		144	

combination of MA and SPS [25–28], but the tensile strength values were not reported.

Herein, for the first time, high-strength Al-based composites reinforced with *h*-BN particles were fabricated from the powder mixtures of individual elements using a combination of HEBM and SPS. The compositions of Al-based multicomponent matrices were selected similar to those of 2xxx and 7xxx series Al alloys widely used in aerospace, automobile, and sport industries.

**Table 1**  
UTS values of Al/BN composites fabricated by different methods.

Composition	Powder mixing technique	Consolidation technique	UTS at room temperature, MPa	UTS at elevated temperature, MPa	Ref.
Al/BN nanotubes (5 wt %)	Ultrasonic assisted wet mixing	High-pressure torsion	384	–	[3]
Al/BN nanotubes (3 wt %)	Wet stirring	High-pressure torsion	304	–	[4]
Al/nano-BN (3 wt%)	Planetary ball milling and annealing	Hot extrusion	333	–	[5]
Al/micro-BN (20 vol%)	Planetary ball milling	Hot pressing sintering and extrusion	230	–	[6]
Al/nano-BN (4.5 wt%)	Ultrasonic assisted wet mixing	Spark plasma sintering	150	119 (300 °C)	[7]
Al/nano-BN (1 wt%)	Ultrasonic assisted wet mixing	Spark plasma sintering	152	–	[8]
Al/micro-BN (4.5 wt%)	High-energy ball milling	Spark plasma sintering	386	141 (500 °C)	[9]
Al/nano-BN (7 wt%)	High-energy ball milling	Spark plasma sintering	385	126 (500 °C)	[9]
Al/micro-BN (5 wt%)	High-energy ball milling	Spark plasma sintering	380	170 (500 °C)	[10]

Cu is a major alloying element in wrought 2xxx series Al alloys, which are easy to heat treat. These materials have high strength at room and elevated temperatures with UTS values in a range of 186–428 MPa, but their corrosion resistance is inferior to other alloys [29]. In contrast, Zn is a major alloying element in 7xxx series Al alloys. These materials are easy to heat treat and mechanically join. They have high UTS values ranging from 221 to 607 MPa [29]. To achieve the desired level of mechanical properties, Al alloys are always subjected to heat treatment or work hardening. Therefore, their UTS depends on the type of post processing.

Application of Al alloys in automotive and aerospace industries requires their thermal stability at elevated temperatures. At temperatures above 150 °C, Al alloys suffer a drastic loss in strength followed by catastrophic softening with increasing temperature. Therefore, the primary goal is to lift their operating temperatures above 400 °C [30].

In the present work, unlike the traditional approach based on heat treatment or work hardening, decently high level of mechanical properties at room and elevated temperature was achieved by adding *h*-BN particles as a reinforcing phase. In addition, Al2xxx and Al7xxx series composite materials were obtained from the elemental powder mixtures by HEBM and subsequent SPS processing to show that such approach is easily scalable. To the best of our knowledge, only simplified (3 elements) Al2xxx series composites without additional additives have so far been obtained by a combination of ball milling and SPS [25].

## 2. Materials and methods

### 2.1. Preparation of powder mixtures

An aluminum powder (ASD-1, Russia), 99% purity and 2.7 g/cm<sup>3</sup> density, consisting of spherical particles with an average size (AS) of 10 μm was used as the basis for 2xxx and 7xxx series Al alloys (Fig. S1a). The alloying elements were: spherical Zn particles, AS = 5 (Alfa Aesar, USA); irregular shape Cu particles, AS = 25 μm (Plasmoetherm, Russia); Mg, AS = 40 μm (Riedel-deHaen, Germany); Si, AS = 10 μm (Plasmoetherm, Russia); Mn, AS = 400 μm (Hongwun, China); Fe, AS = 30 μm (Labtech, Russia); Cr, AS = 10 μm (Plasmoetherm, Russia); Ti, AS = 20 μm (Plasmoetherm, Russia) (Figs. S1b–i). A commercial BN flake powder (Reachem, Russia) of chemical grade with a density of 2.3 g/cm<sup>3</sup> was used as a reinforcing additive to the Al-based composites. The flakes had an AS of 5–10 μm and a thickness of 0.2–0.5 μm (Fig. S1j).

Al-based master powders for SPS were lab-made by adding various alloying elements (Table 3) to the Al powder and mixing using a ball-mill mixer E<sub>max</sub> (Retsch GmbH, Germany) with ZrO<sub>2</sub> jars and balls in an Ar atmosphere (99.998%, OOO «PGC-service», Russia) to prevent oxidation. The mixing process was carried out in three stages: at 300 rpm for 30 min to homogenize the mixture, at 500 rpm for 30 min to perform dynamic mixing, and HEBM at 800 rpm for 120 min to proceed with mechanical alloying. Finally, BN particles were added in the amounts of 1, 3, and 5 wt% and the resultant powders were mixed under an Ar atmosphere at 800 rpm for 120 min.

### 2.2. Synthesis of composite materials by spark plasma sintering

Al-based master mixtures with and without BN additives were consolidated in graphite dies by SPS using a LABOX 650 press and an auxiliary sintering equipment (SINTER LAND Inc., Japan). The sintering process was carried out in forevacuum (40 Pa) as described elsewhere [9]. Sintering temperature (as controlled by a thermocouple) was 625 °C

that is close to the melting point of Al. The applied pressure and holding time were 38.55 MPa and 60 min, respectively. In order to prepare samples for tensile tests, SPS samples were cut into 28–34 mm long stripes using a Secotom-50 cutting machine (Struers Inc., Denmark), polished, and finally dog-bone shaped (Fig. S2) by using a CHMER GX-320L electrical erosion cutting machine (Taiwan).

### 2.3. Tensile tests

Tensile tests at room temperature (RT) and elevated (350 and 500 °C) temperatures were carried out using an universal Shimadzu AG-X Series testing machine (Shimadzu Corp., Japan) equipped with a high-temperature furnace. For each composition, four samples were tested. Samples were loaded at a strain rate of  $6.6 \times 10^{-5}$  m/s until their complete failure. The strain values and strain rates were measured using an extensometer.

### 2.4. Hardness measurements

Hardness of composite materials was measured by the Vickers method on an automatic DuraScan 70 microhardness tester (EMCO-TEST Prüfmaschinen GmbH, Austria) according to ISO 6507 standard [31]. For each sample, an average value was determined based on five independent measurements.

### 2.5. Density measurements

An hydrostatic weighing method was used to estimate the density of composites according to ISO 3369:2006 standard [32].

### 2.6. X-ray diffraction

X-ray diffraction (XRD) patterns of the composites were recorded on a diffractometer DIFRAY-401 (Scientific Instruments, Russia) equipped with a position sensitive detector (Elion) using the Bragg-Brentano geometry. The shooting was carried out in the step scan mode in the 2θ range of 10°–80° at a scan step of 0.1° and exposure time of 4 s.

### 2.7. Scanning electron microscopy

Microstructures of powder mixtures and SPS composite materials, as well as their fracture surfaces after the tensile tests were studied by means of scanning electron microscopy (SEM) on a JSM F7600 instrument (JEOL Ltd, Japan) equipped with a backscattered electrons detector and an OXFORD X-Max 80 energy dispersive X-ray (EDX) spectrometer (Premium, England). The SEM analysis was performed under accelerating voltage of 5–15 kV.

### 2.8. Transmission electron microscopy

Samples for transmission electron microscopy (TEM) were prepared using a focused ion beam (FIB) on a S8000Xe Plasma FIB-SEM instrument (TESCAN, Czech Republic). "High-resolution structural analysis and spatially-resolved elemental mapping were carried out on a JEM-2100 transmission electron microscope (JEOL Ltd., Japan)".

### 2.9. Grain size evaluation

The samples were polished, etched by a Weck's reagent (SPS-

**Table 3**  
Compositions of the Al matrices.

Elements in wt.%	Al	Zn	Mg	Cu	Fe	Si	Mn	Ti	Cr
Al7	rest	5.1	2.1	1.2	~0.2	~0.05	~0.02	~0.02	~0.18
Al2	rest	~0.02	~0.2	3.9	~0.2	0.5	0.4	~0.02	~0.02

fabricated composites) and a Keller's reagent (powder mixtures after HEBM), and investigated with an optical microscope (Olympus, Japan). The grain size was determined using an ImageJ particle's measuring tool.

## 2.10. Atomistic simulations

Classical molecular dynamics (MD) simulations were carried out to estimate critical shear stress between polycrystalline Al nanoparticles with and without *h*-BN intermediate layers. Interaction between Al nanoparticles was described by the embedded-atom method (EAM) potential [33] parameterized by Zhou et al. [34]. The behavior of *h*-BN monolayer was described by Tersoff many-body potential parameterized for B-N-C compounds [35]. The interaction between Al nanoparticles and *h*-BN intermediate layers was described by means of the Lennard-Jones 12-6 potential. Empirical parameters were fitted to obtain correct description of the critical shear stress value which is consistent with the earlier Density Functional Theory (DFT) results [36] under considering Van der Waals corrections [37]. Interaction parameters were defined as  $\epsilon = 0.014$  eV and  $\sigma = 3.52$  Å. For fitting of interatomic potential see Supporting Information (description and Fig. S3). Fitted parameters show the critical shear stress value of about 10 MPa, that is consistent with the early DFT results [37]. All the simulations were performed using a LAMMPS [38] program package with the periodic boundary conditions in the XY plane.

## 3. Results

### 3.1. Microstructure of raw materials

Al-based powder mixtures (hereafter denoted as Al7 and Al2) with compositions corresponding to those of Al7075 and Al2014 alloys (Table 3) were lab-fabricated by HEBM. BN particles at the amounts of 1, 3, and 5 wt% were added to the Al-based powder mixtures and homogenized by HEBM. SEM images of raw Al2 and Al7 powder mixtures with and without BN additives after HEBM processing are shown in

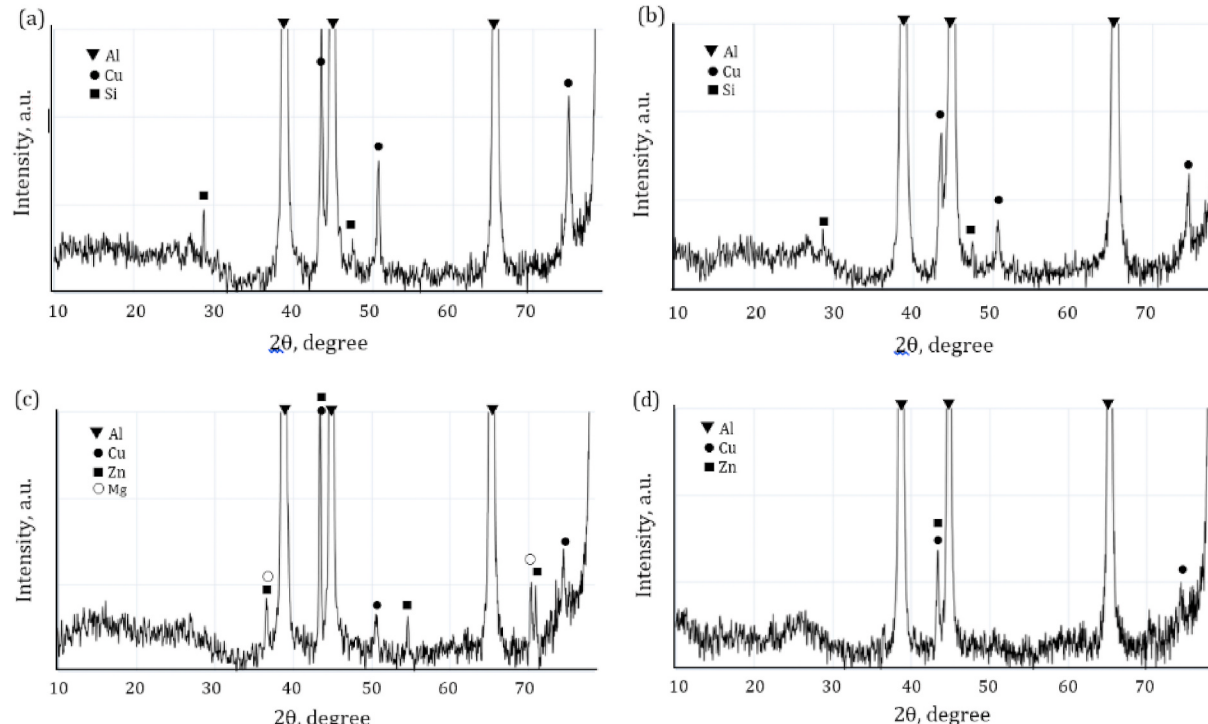


**Fig. 1.** XRD patterns of Al2 (a), Al2-3%BN (b), Al7 (c), and Al7-3%BN (d) mixtures after ball milling.

**Fig. S4.** After adding BN particles, the surface has a flaky appearance due to lubricating characteristics of *h*-BN (Figs. S4c and d).

XRD patterns of Al2, Al7, Al2-3%BN, and Al7-3%BN mixtures after ball milling are presented in Fig. 1. All observed peaks are attributed to the individual elements and no additional compounds (due to their chemical interaction during HEBM) are observed. In Al2 composites, the main elements are Al, Cu, and Si, which is in a good agreement with the nominal material composition (Table 3). The XRD pattern of sample A7 reveals the presence of Al, Cu, Zn, and Mg. It is noteworthy that the Mg peaks became weaker when the BN phase had been added. This observation suggests either Mg and BN interaction or dissolution of Mg into the Al matrix.

### 3.2. Microstructure of composite materials after SPS

#### 3.2.1. Al grain size

To determine the Al grain size, the SPS-produced composites were polished, etched, and analyzed in an optical microscope. The obtained values are presented in Table 4. Considering that the average particle size of the initial Al powder was 10 µm, it can be concluded that several Al particles had formed one grain during SPS. The average Al grain size in Al7 and Al7-3%BN samples was almost 2 times smaller compared with Al2 and Al2-3%BN materials (Table 4).

The phase formation in the multicomponent systems, such as 2xxx and 7xxx series Al composites, is a rather complicated process. During sintering, various Al-, Fe-, and Cu-based intermetallic phases can be formed. In addition, Mg can be oxidized and BN additives can react with Al matrix to form AlN and AlB<sub>2</sub> phases. Thus, to establish the phase compositions of Al-based composites as accurately as possible, the

**Table 4**

Average Al grain size after SPS.

Sample	Al2	Al2-3%BN	Al7	Al7-3%BN
Grain size, µm	60	65	38	36

materials were characterized using several analytical techniques, such as XRD, SEM/EDS, and high-resolution TEM.

### 3.2.2. X-ray diffraction

Besides metallic Al, the XRD pattern of Al2 composite reveals the presence of tetragonal Al<sub>2</sub>Cu and cubic AlCu<sub>3</sub> phases (Fig. 2a). After adding BN phase, only the cubic AlCu<sub>3</sub> phase is observed (Fig. 2b). In Al7 composite, the material microstructure is more complicated: Al<sub>2</sub>Cu (tetragonal), AlCu<sub>3</sub> (orthorhombic), and Al<sub>5</sub>Cu<sub>6</sub>Mg<sub>2</sub> (cubic) phases are present (Fig. 2c). For the Al7–3%BN material, except three main XRD peaks from metallic Al, no other well-defined peaks are seen (Fig. 2d).

### 3.2.3. Microstructure of composites

SEM images of the Cu-containing intermetallic particles (according to XRD data) precipitated inside the Al grains are shown in Fig. S5. The particles appear white in color. They are homogeneously distributed within the Al matrix. Most of the observed particles in Al2 composites are 1–2 µm in dimensions, although individual particles or their agglomerates have a size of up to 5 µm (Figs. S5a and b). In Al7 composites, the reinforcing particles are smaller and their size ranges from 60 to 200 nm (Figs. S5c and d). In BN-containing materials, a bimodal size distribution is seen, i.e., many nanoparticles are smaller than 100 nm (Al2-BN) and 30 nm (Al7-BN).

### 3.2.4. SEM/EDS analysis

SEM images and corresponding EDS elemental maps of an Al2 composite are illustrated in Fig. 3. EDS analysis suggests the presence of globular Cu-rich (~500 nm in size) and needle/plate-like Cu-containing (several µm in length) particles (AlCu<sub>3</sub> and Al<sub>2</sub>Cu according to XRD data) and Mg oxide inclusions mostly precipitated along the Al grain boundaries. Al-based metallic matrix contains Cu, Mg, Mn, Si, and Fe elements hereby indicating the formation of an Al(Mg,Si,Mn,Fe,Cu) solid solution.

In the case of Al2–3%BN composite, two main phases can be distinguished in the corresponding SEM/EDS images (Fig. 4): Al(Mg,Si,Mn,Fe,Cu) solid solution and a Cu-containing phase enriched in Al.

SEM/EDS analysis also suggests the presence of small AlB<sub>2</sub> (~300 nm) and Si<sub>3</sub>N<sub>4</sub> (~100 nm) inclusions (Fig. S6).

SEM/EDS analysis of Al7 sample indicates the formation of Al(Cu,Zn,Mg) solid solution and Cu- and Fe-rich intermetallic phases (Fig. 5). The AlCu<sub>x</sub> particles have a white contrast and their size ranges from 20 to 90 nm (Figs. 5a and S7). A Fe-rich (Fe,Al,Cu) precipitate, approximately 100 × 600 nm<sup>2</sup> in dimensions, has a plate-like morphology (Fig. 5b). In addition, numerous MgO<sub>x</sub> particles of dark-grey contrast are observed to precipitate along the Al grain boundaries (Fig. S7).

After adding BN phase, the corresponding spatially-resolved EDS elemental maps (Fig. 6a) suggest the precipitation of the following phases: BN (area 5), BNO (area 4), MgB<sub>x</sub> (areas 1), MgO<sub>x</sub> (area 3), MgNO (area 2). The EDS analysis of other sample areas reveals the presence of AlCu<sub>3</sub> and MgB<sub>x</sub> inclusions (Fig. 6b). The size of precipitates ranges from 100 to 300 nm.

### 3.2.5. High-resolution TEM

More detailed information on the composite microstructures and the types of smallest inclusions was obtained through analyzing high-resolution TEM images, Inverse Fast Fourier Transform (IFFT) images and Fast Fourier Transform (FFT) patterns. In Al2 and Al2–3%BN samples, Al<sub>5</sub>Cu<sub>6</sub>Mg<sub>2</sub> and Al<sub>6</sub>CuMg<sub>4</sub> inclusions are observed (Fig. 7a–c, e). They either have a plate-like single-crystalline morphology with a width of approximately 30–50 nm; or are formed by several sub-grains, several nm in size (Fig. 7e). The MgO<sub>2</sub> precipitates are typically 10–20 nm in dimensions and consist of sub-grains (Fig. 7d).

The presence of AlCu<sub>3</sub> (Fig. 8a), Al<sub>2</sub>Cu/Fe<sub>3</sub>Al (Fig. 8b and c), Al<sub>5</sub>Cu<sub>6</sub>Mg<sub>2</sub> (Fig. 8d), and MgO<sub>2</sub> (Fig. 8e) phases in A7 composites was also confirmed by high-resolution TEM imaging and corresponding FFT patterns. Precipitates are rather small, c.a. 10–50 nm in dimensions. The AlCu<sub>3</sub> and Al<sub>2</sub>Cu/Fe<sub>3</sub>Al crystallites have a plate-like morphology and often exhibit well-defined sharp interfaces, whereas the Al<sub>5</sub>Cu<sub>6</sub>Mg<sub>2</sub> and MgO<sub>2</sub> particles are globular or irregular in shape. In addition to phases mentioned above, the TEM study revealed the presence of Al<sub>4</sub>Cu<sub>9</sub> inclusions (Fig. 9). They are mostly precipitated along Al grain boundaries as irregularly shaped particles, 100–200 nm in size, but sometimes take

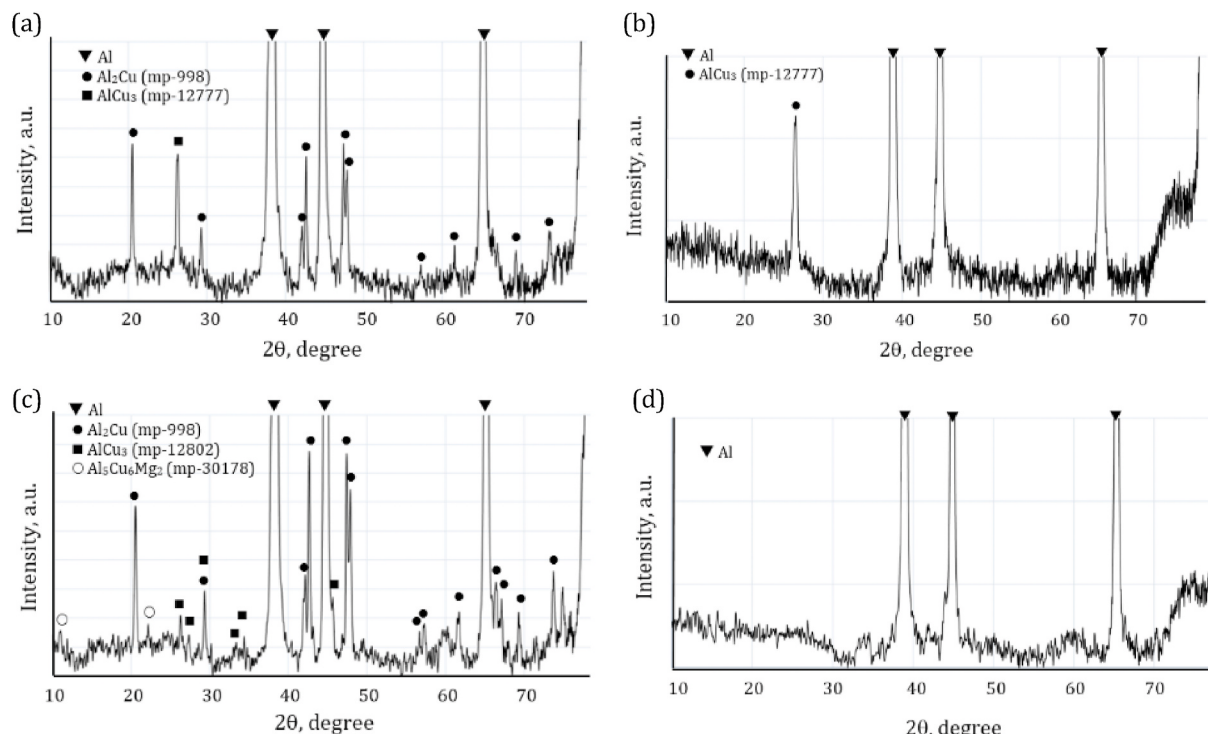


Fig. 2. XRD spectra of Al2 (a), Al2–3%BN (b), Al7 (c), and Al7–3%BN (d) composites after SPS.

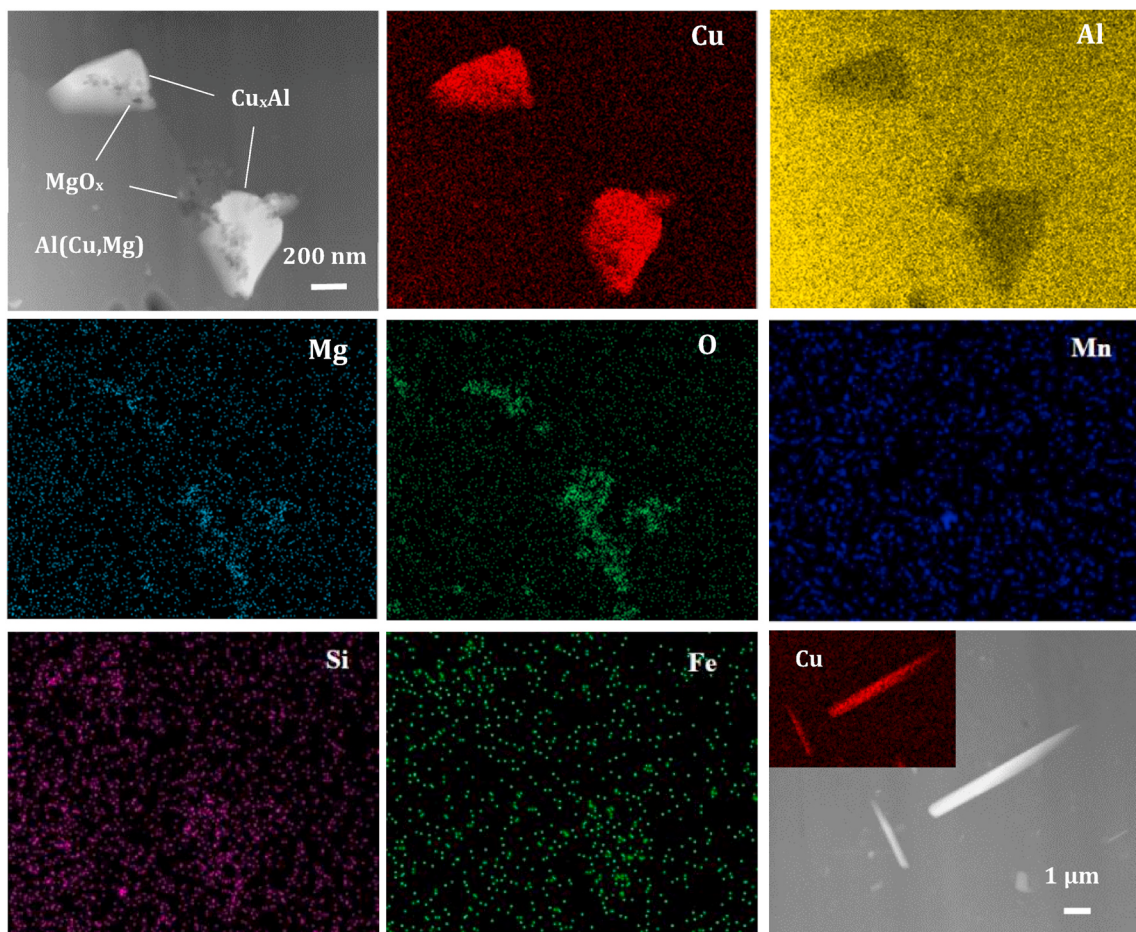


Fig. 3. SEM images and corresponding EDS elemental maps of Al2 composite.

a plate-like form and precipitate within the Al grains (Fig. 9b).

The typical TEM micrograph of Al7–3%BN composite is shown in Fig. 10a. Numerous nanoparticles, 5–50 nm in dimensions, with spherical, elongated, and plate-like morphologies were formed both inside the Al grains and along their grain boundaries. These were identified as  $MgB_4$  (Fig. 10b,d) and  $Mg_3(BO_3)_2$  (Fig. 10c). These inclusions have clear edges on which growth ledges are also observed. Inside the Al-based matrix, small  $h$ -BN inclusions, several nm in size, are seen (Fig. 10e).

### 3.3. Composite density and mechanical properties

Fig. S8 illustrates the change in porosity of Al7 and Al2 composites with increasing BN content. The minimal porosity was in the samples with 1 wt% of BN. At 3 wt% of BN, the porosity of Al7 composite was lower compared with the BN-free composite, whereas the porosity of BN-doped Al2 sample slightly increased.

The Vickers hardness values of Al2, Al7, Al2–3%BN, and Al7–3%BN composites are presented in Fig. S9. The initial hardness of BN-free Al7 sample (97 HV) is approximately 22% higher than that of its Al2 counterpart (76 HV). All the BN-doped samples demonstrated the increased hardness. At 3 wt% of BN, the hardness is 130 HV (Al7-BN) and 123 HV (Al2-BN). Interestingly, at 3 and 5 wt% of BN the difference in hardness between samples Al2-BN and Al7-BN becomes less than 5%.

The results of tensile tests at room temperature (RT) are shown in Fig. 11a and b. All the BN-containing composites demonstrate an increase in strength compared with pure Al2 and Al7 samples. The maximum tensile strength of 310 MPa (Al7-BN) and 235 MPa (Al2-BN) is documented for samples with 3 wt% of BN, which corresponds to a strength increase of approximately 74% and 16%, respectively. With a

further increase in the amount of BN additives up to 5%, the strength deteriorates; however, the composite strength values are still 53% and 8% higher than those of the BN-free samples.

Fig. 11c and d illustrates the results of tensile tests carried out at elevated temperatures. At 350 °C, the tensile strength values are 227 MPa (Al2 series) and 276 MPa (Al7 series). Thus, compared to RT, the strength values at 350 °C decrease by only 3% (Al2–3%BN) and 11% (Al7–3%BN). A substantial increase in tensile strength (~40%) at 500 °C is observed for both sample series: from 130 MPa (pristine Al7) to 187 MPa (Al7–3%BN) and from 150 MPa (pristine Al2) to 221 MPa (Al2–3%BN). Note, that Al2–3%BN and Al2–5%BN composites have almost similarly high strength at 500 °C, they also demonstrate the improved high-temperature ductility, as evidenced by a shape of stress-strain curves (Fig. 11d). It is also important to emphasize the difference in Al2 and Al7 composite strength at 25 and 500 °C. While at RT the maximum strength of the best A7 sample series with 3 wt% of BN is 32% higher compared with Al2–3%BN counterpart, at 500 °C the tensile strength of Al7–3%BN is 22% lower. Compared to RT, the tensile strength at 500 °C is reduced by 40% for Al7 and only 6% for Al2. Summing up, adding 3 wt% of BN particles increases the tensile strength by 16% (25 °C) and 40% (500 °C) for Al2 composite and by 74% (25 °C) and 40% (500 °C) for Al7 sample. Fig. 11e compares the strength values of our best samples at different temperatures with the available literature data. The UTS values of many Al-based composites rapidly decrease with increasing temperature (as schematically shown by black dotted line in Fig. 11e). Although the RT strength of the Al2–3%BN and Al7–3%BN composites is not the highest, they show considerably higher strength above 300 °C (area indicated by a purple circular dotted line). Of particular note is Al2 series sample with the almost constant strength

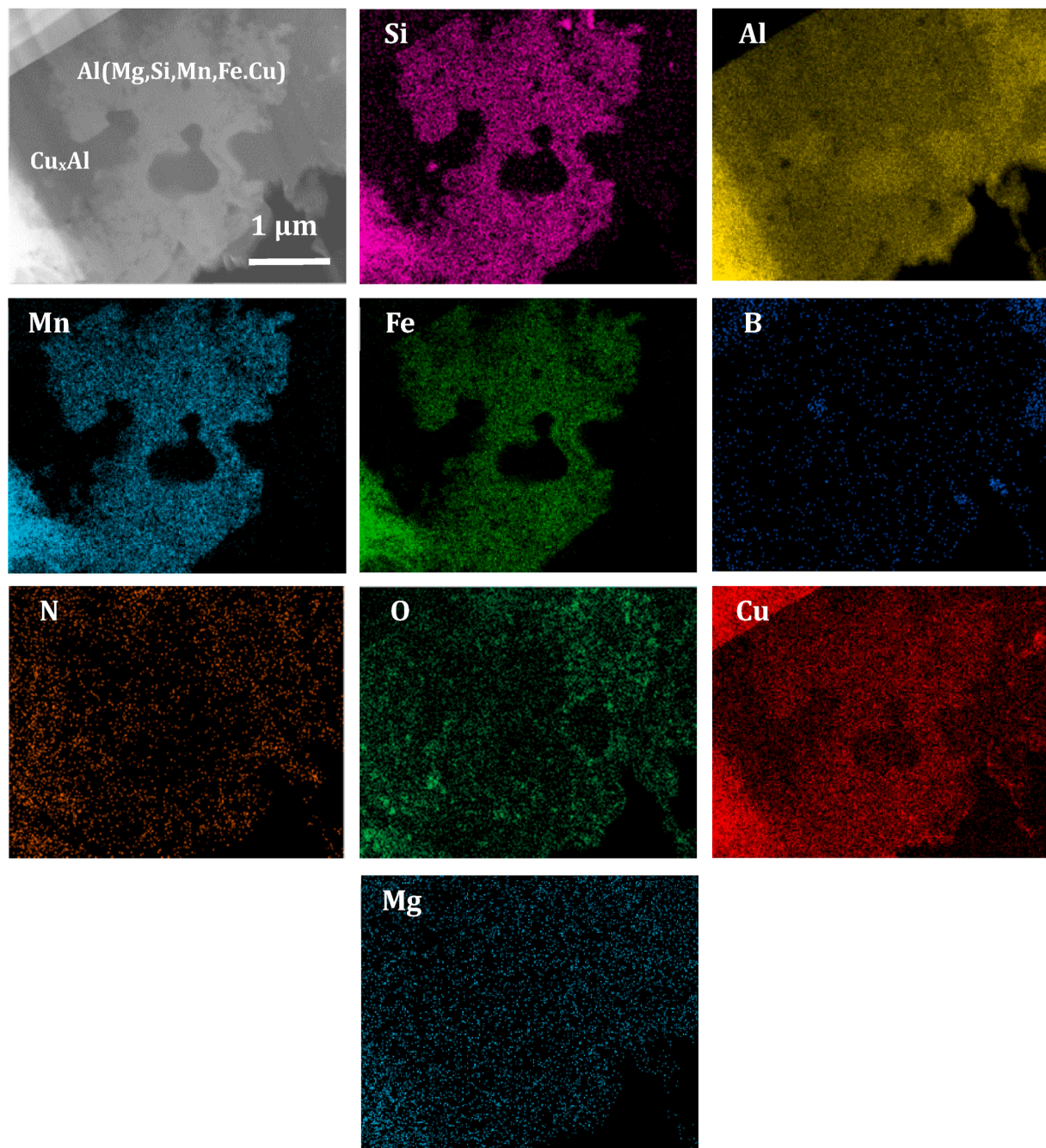


**Fig. 4.** SEM image and corresponding EDS elemental maps of Al2–3%BN composite.

in the temperature range of 25–500 °C (blue dotted line). Thus, our results open up new possibilities for the fabrication of Al-based composite materials for applications at elevated temperatures.

#### 3.4. Microstructure of fractured surface

SEM fracture micrographs of the BN-free and BN-added samples with 3 wt% of BN after RT tensile tests are shown in Fig. 12. Although fracture surfaces of pristine Al2 (Fig. 12a,c) and Al2–3%BN (Fig. 12b) samples reveal a fine web-like morphology with numerous dimples, which is commonly believed to be an evidence of local plastic deformation, the BN-free and BN-doped materials do not reveal strain hardening regions on the stress-strain curves. It is supposed that the large cells observed in the BN-containing composites had been formed due to a higher stress concentration than in the pure Al2 material and dislocations' collapse

into microvoids. Material delamination is also seen within the fracture area (shown by a double arrow in Fig. 12d) indicating grain boundary cracking during deformation. The exposed fracture surface is densely populated with firmly adhered reinforcing nanoparticles (shown by a single arrow in Fig. 12d). This indicates strong chemical/mechanical bonding at the particle/matrix interfaces.

Alternation of large smooth and dimpled areas on Al7 sample fracture surface indicates a combination of brittle and ductile fractures (Fig. 12e). Al7–3%BN composite demonstrates a rough formless surface morphology more typical for a brittle fracture (Fig. 12f). Inside a large pore, the network of smaller cells is clearly seen (Fig. 12h). The observation that the fracture structures of Al7 and Al7–3%BN samples are more diverse than those of Al2 and Al2–3%BN counterparts is in a good agreement with the stress-strain curve shapes presented in Fig. 11a and b.

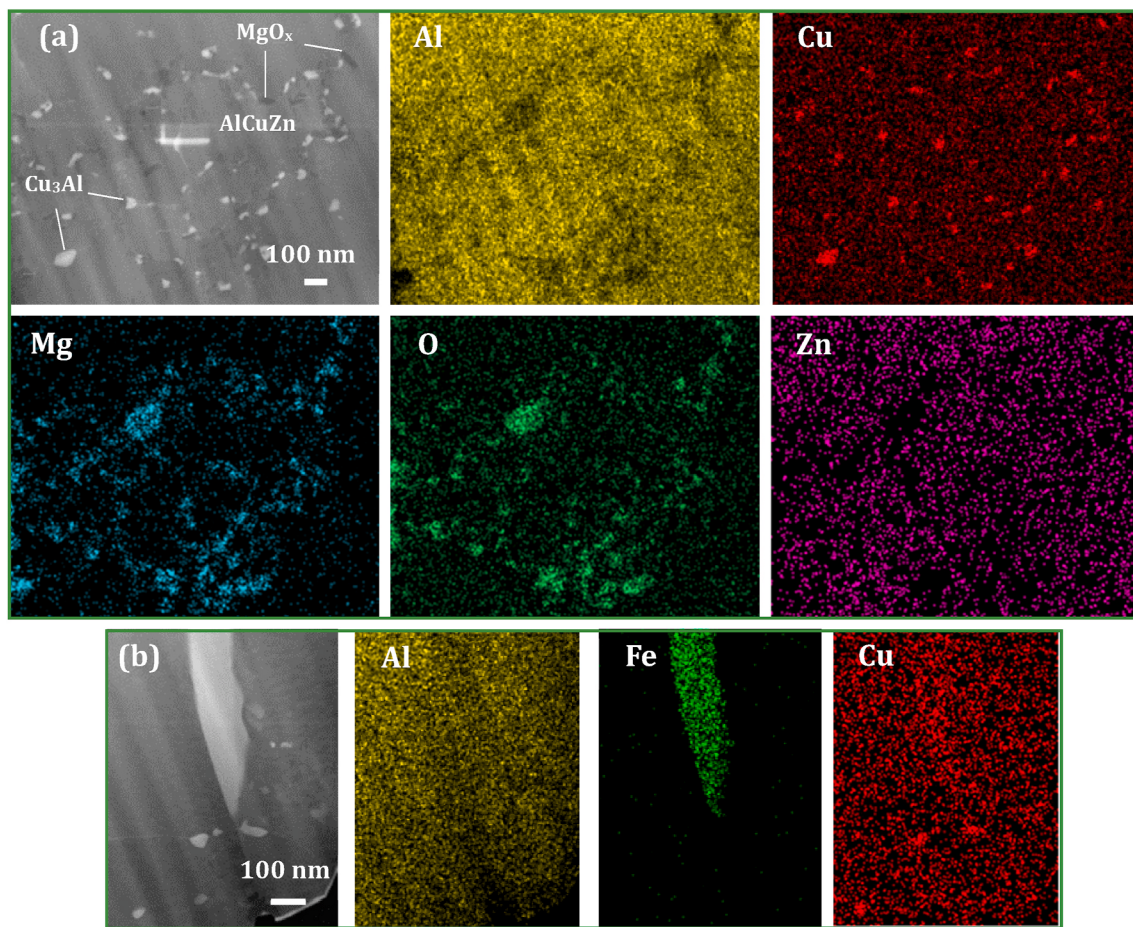


**Fig. 5.** SEM images and corresponding EDS elemental maps of Al7 composite.

The fracture surface of Al2 sample after the tensile tests at 500 °C was similar to that observed after RT test. It is relatively uniform revealing dense cellular and web-like structures (Fig. 13a). In contrast, the fracture surface of Al2–3%BN material reveals bimodal size cell distribution. Large cells approximately 10–15  $\mu\text{m}$  in diameter are seen to be surrounded by the network of smaller cells, 1–3  $\mu\text{m}$  in dimensions (Fig. 13b). This dimpled structure is in a good agreement with the characteristic distances between reinforcing inclusions (Fig. S4), which supports the conclusion of Broek [39] that ductile rupture initiates at small inclusions and the average spacing between dimples is equal to the average inclusion distance. Inside deep and well-defined dimples, numerous reinforcing nanoparticles are observed. No nanoparticle decohesion from the Al matrix is seen on the fracture surface indicating good nanoparticle/matrix bonding. These nanosized particles serve as effective barriers against dislocation motion and enhance the high-temperature strength.

Al7 composite predominantly reveals an intergranular fracture (Fig. 13d). Flat fracture areas alternating with cellular structure indicate a combination of ductile and brittle fractures (Fig. 13e). The stress-strain curve presented in Fig. 11c reveals all characteristic stages of a ductile material (linear part, strain hardening and necking). Interestingly, the Al7–1%BN composite showed almost similar mechanical behavior under tension. The Al7–3%BN composite fails while the deformation is mostly elastic. The network of fine cells is observed in the Al7–3%BN material after tensile deformation at a high temperature (Fig. 13f).

## 4. Discussion

### 4.1. Microstructure and phase composition

Summarizing the XRD, SEM/EDS, and high-resolution TEM data, the phase compositions of Al2, Al7, Al2–3%BN, and Al7–3%BN samples can be understood (Table 5). The EDS analysis indicates that Al-based solid solution in Al2 samples contains Cu, Fe, Mn, Mg, and Si. The Al matrix in A7 composite contains Cu, Zn and Mg. The room temperature solubility of Zn, Mg and Cu atoms in Al is low [28]:  $\leq 0.01$  wt% for Cu [40],  $\leq 0.1$  wt% for Zn [41], and  $\leq 1.8$  wt% for Mg [42]. The maximum solubility of Cu in Al is 2.5 at.% at the eutectic temperature of 550 °C [43], but as predicted based on the microscopic electronic theory [44], may increase under high pressure. The low solubility of Cu in Al is due to the difference in valences of the solvent and solute atoms [45]. The maximum solubility of Si in Al is 1.65 wt% at the eutectic temperature of 577 °C [46], but can increase to 15 at.% at high pressure (54 kbar) [47]. In contrast, the solubility of other alloying elements at elevated temperatures is higher: 20 at.% (Mg) and 5.5 at.% (Fe) [45]. During SPS at  $\sim 625$  °C (a value close to the melting point of Al) the formation of supersaturated solid solution with immiscible components is quite possible. For example, a supersaturated solid solution of Cu in Al was reported for an Al-4.5Cu composite after ball milling [48].

The XRD data indicate that the intermetallic  $\text{AlCu}_3$  and  $\text{Al}_2\text{Cu}$  grains are the main secondary phases in Al2 and Al7 composites. The interdiffusion between Al and Cu atoms at the Al/Cu interface in the

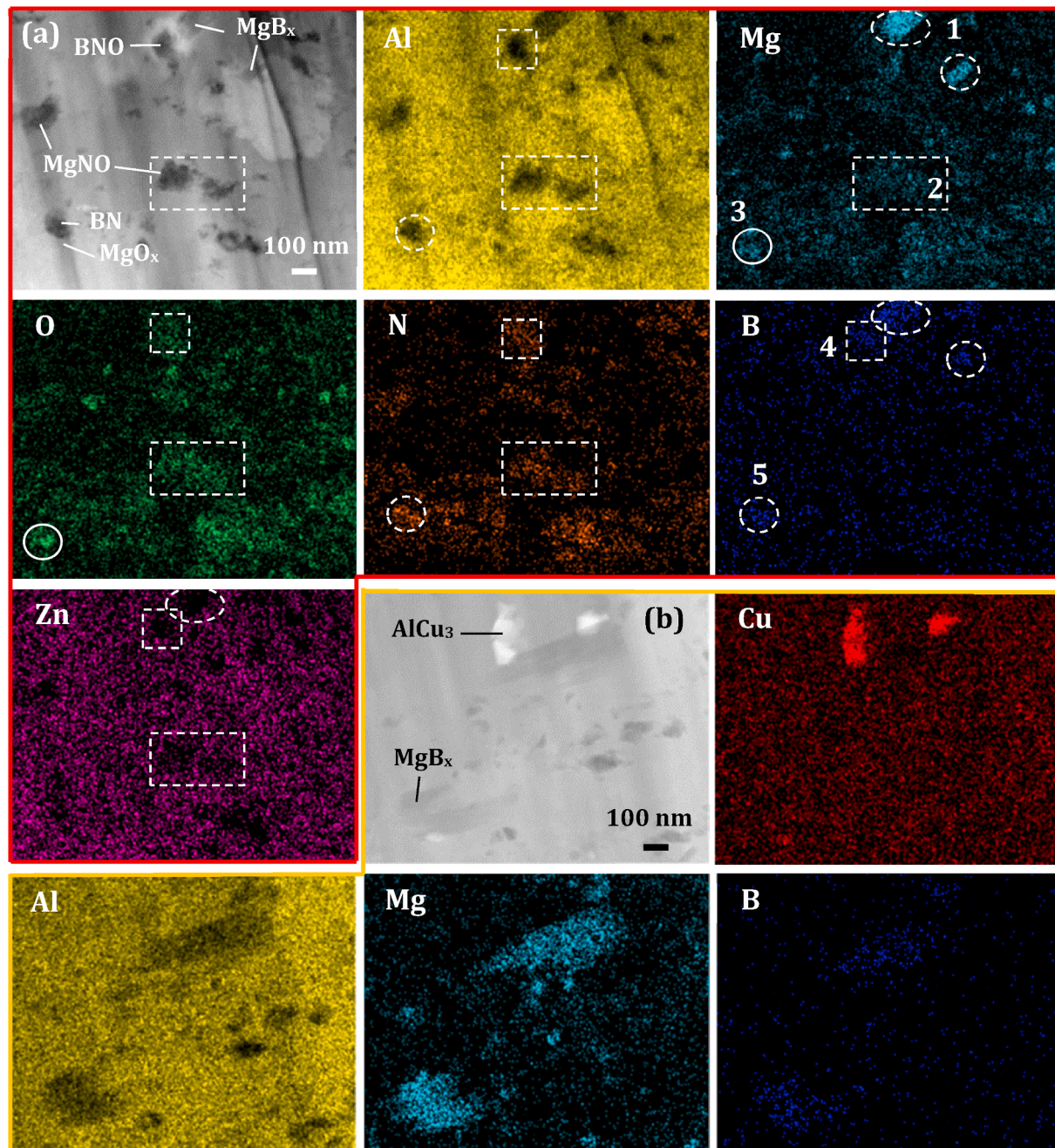


**Fig. 6.** SEM images and corresponding EDS elemental maps of Al7–3%BN composite.

temperature range of 375–450 °C is very intense; the interdiffusion coefficients could reach  $7.8 \times 10^{-12} \text{ m}^2/\text{s}$  [49]. Formation of an Al<sub>2</sub>Cu phase has previously been reported in an Al–20Cu–15Mn composite fabricated through blending and sintering [23] and an Al–7Zn–2.5Mg–2.5Cu alloy prepared via mechanical alloying and SPS [25].

Detailed SEM/EDS and high-resolution TEM analyses also reveal small inclusions of Mg oxide (Al<sub>2</sub>, Al<sub>7</sub>) and a single Fe-rich Fe(Al,Cu) precipitates (Al<sub>7</sub>). The MgO<sub>x</sub> phases frequently form at high temperatures due to high affinity of Mg to oxygen. No Fe-based intermetallic phases were observed in the Al<sub>2</sub> composite with 0.5 wt% of Si. This is in a good agreement with the previous results [50]; in fact, Si addition into Al–Cu–Mn–Fe alloys suppresses the formation of Fe-rich intermetallic phases. The presence of three-component intermetallic phases Al<sub>5</sub>Cu<sub>6</sub>Mg<sub>2</sub> and Al<sub>6</sub>CuMg<sub>4</sub> was confirmed by high-resolution TEM.

During SPS, one part of BN additives reacts with Al, Si, and Mg to form AlB<sub>2</sub>, SiN<sub>x</sub>, and MgB<sub>2</sub>/Mg<sub>3</sub>(BO<sub>3</sub>)<sub>2</sub> phases, while the other part remains unreacted and contributes to the material strength.

The results presented in Table 5 clearly indicate that the phase compositions of Al<sub>2</sub> and Al<sub>7</sub> materials fabricated in the present study (from the powder mixtures of individual elements using a combination of HEBM and SPS) are different from those usually observed for Al2014 and Al7075 alloys manufactured by casting and subsequent heat treatment. Except the θ-phase (Al<sub>2</sub>Cu) phase, we do not observe (Mn,Fe)<sub>3</sub>S<sub>6</sub>iAl<sub>12</sub>, Cu<sub>2</sub>Mg<sub>8</sub>Si<sub>6</sub>Al<sub>5</sub>, Cu<sub>2</sub>Mn<sub>3</sub>Al<sub>20</sub>, and Mn<sub>3</sub>SiAl<sub>12</sub> phases frequently reported for the A2014 alloys [51]. Note that columnar grains and dendrites, which are often observed in solidified Al [52–54], do not form.

The structure of Al7075 alloy is different after casting ((Fe, Cr)<sub>3</sub>SiAl<sub>12</sub>, Mg<sub>2</sub>Si, and pseudobinary eutectic: Al + MgZn<sub>2</sub> (also referred

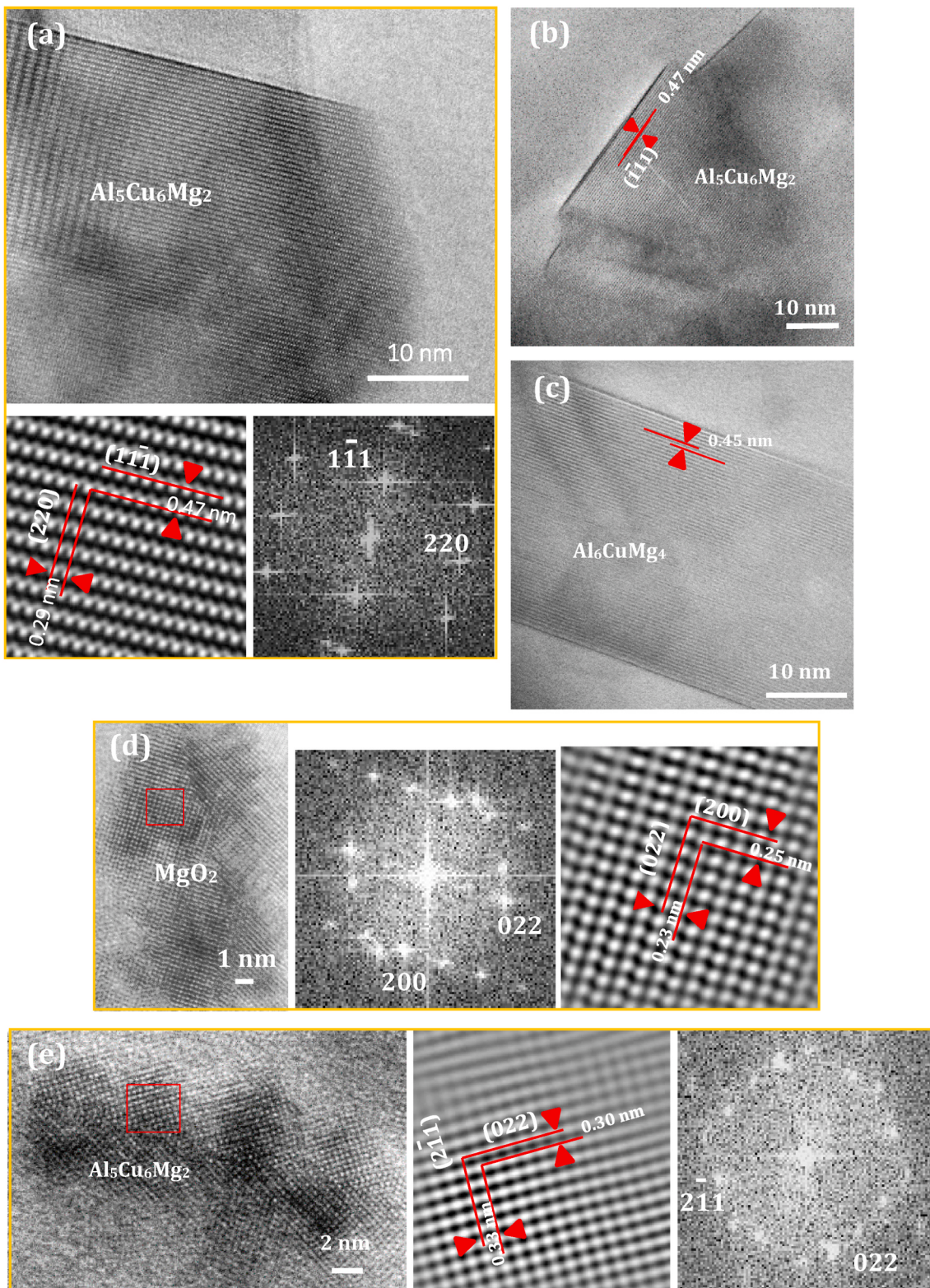


**Fig. 7.** High-resolution TEM micrographs with corresponding FFT and IFFT (filtered HRTEM) images showing  $\text{Al}_5\text{Cu}_6\text{Mg}_2$  (a, b, e),  $\text{Al}_6\text{CuMg}_4$  (c), and  $\text{MgO}_2$  phases (d) in  $\text{Al}2$  (a, b) and  $\text{Al}2\text{-}3\% \text{BN}$  (c-e) composites.

to as  $\text{Mg}(\text{Zn}, \text{Cu}, \text{Al})_2$  and subsequent heating ( $\text{Al}_7\text{Cu}_2\text{Fe}$ ,  $\text{Mg}_2\text{Si}$ ,  $\text{Al}_2\text{CuMg}$ , and  $\text{Cr}_2\text{Mg}_3\text{Al}_{18}$ ). None of these phases were observed after HEBM + SPS processing. This is due to a fact that the phase formation conditions significantly differ at various types of heat treatments. The HEBM process provides uniform element mixing and the subsequent

phase transformations occur in a solid state (SPS is carried out at a temperature below the melting point of Al). Note that we did not observe  $\text{MgZn}_2$  precipitates frequently reported for Al-Zn-Mg composites [25, 27, 55, 56]. According to our results, all Zn was dissolved in a metallic matrix forming an  $\text{Al}(\text{Cu}, \text{Zn}, \text{Mg})$  solid solution.

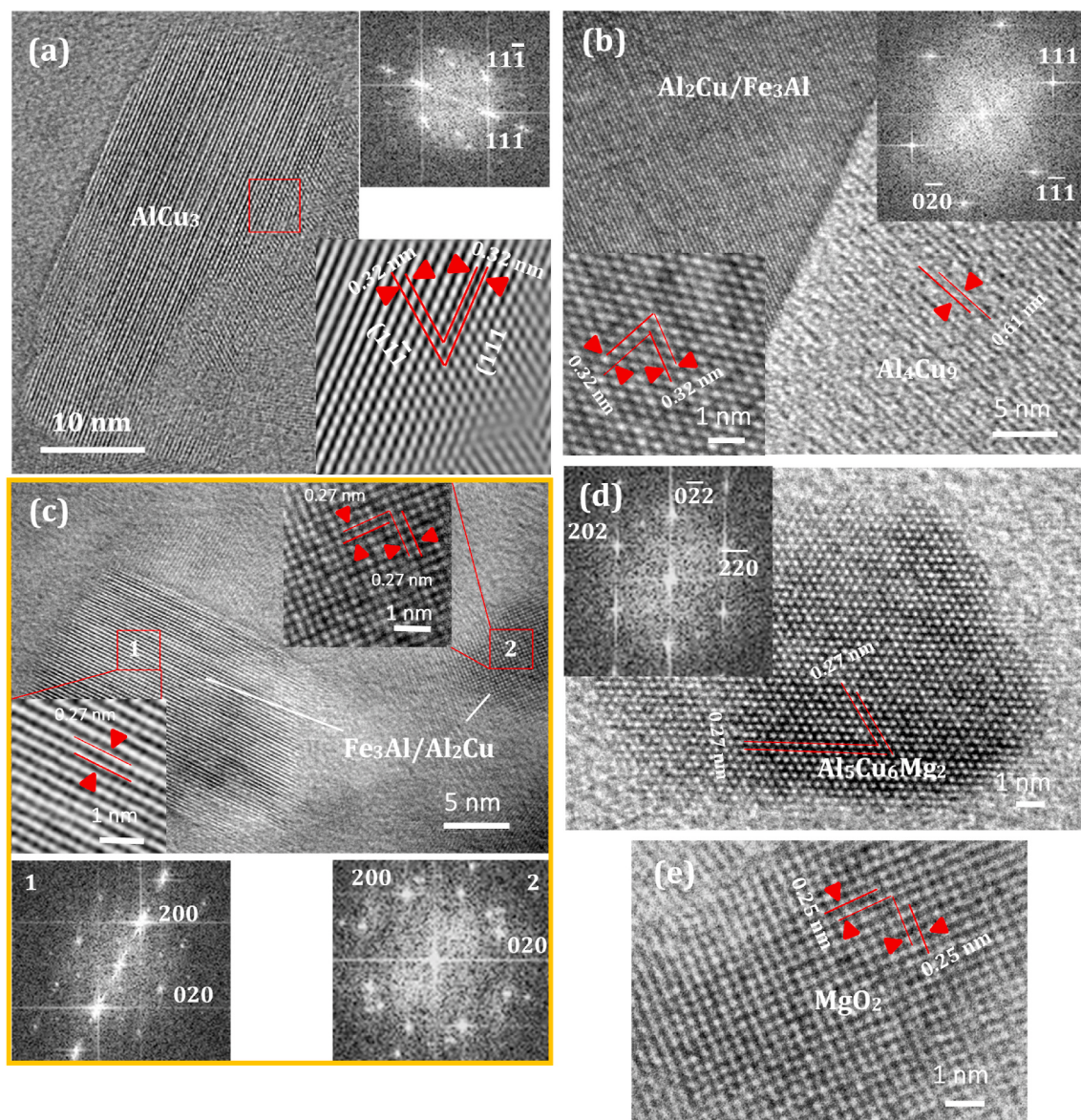


**Fig. 8.** High-resolution TEM micrographs with corresponding FFT and IFFT images showing the presence of AlCu<sub>3</sub> (a), Al<sub>2</sub>Cu/Fe<sub>3</sub>Al (b,c), Al<sub>5</sub>Cu<sub>6</sub>Mg<sub>2</sub> (d) and MgO<sub>2</sub> phases in Al7 composite.

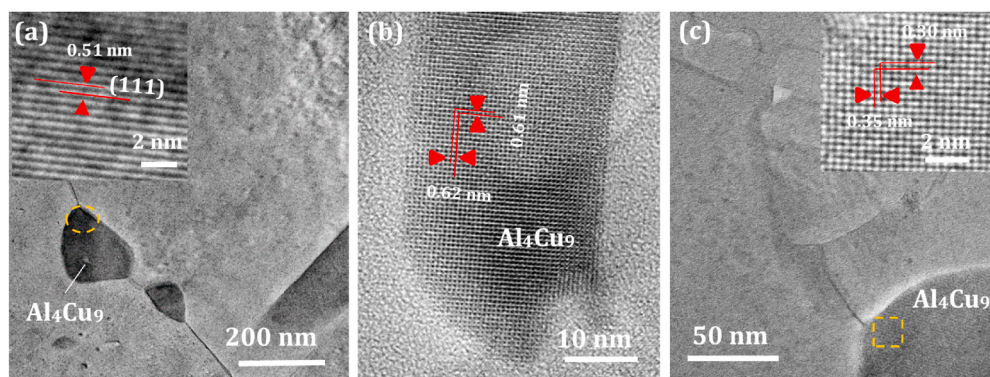


**Fig. 9.** TEM (a, c) and high-resolution TEM images (b, insets in (a) and (c)) showing Al<sub>4</sub>Cu<sub>9</sub> grains in Al7 composite.

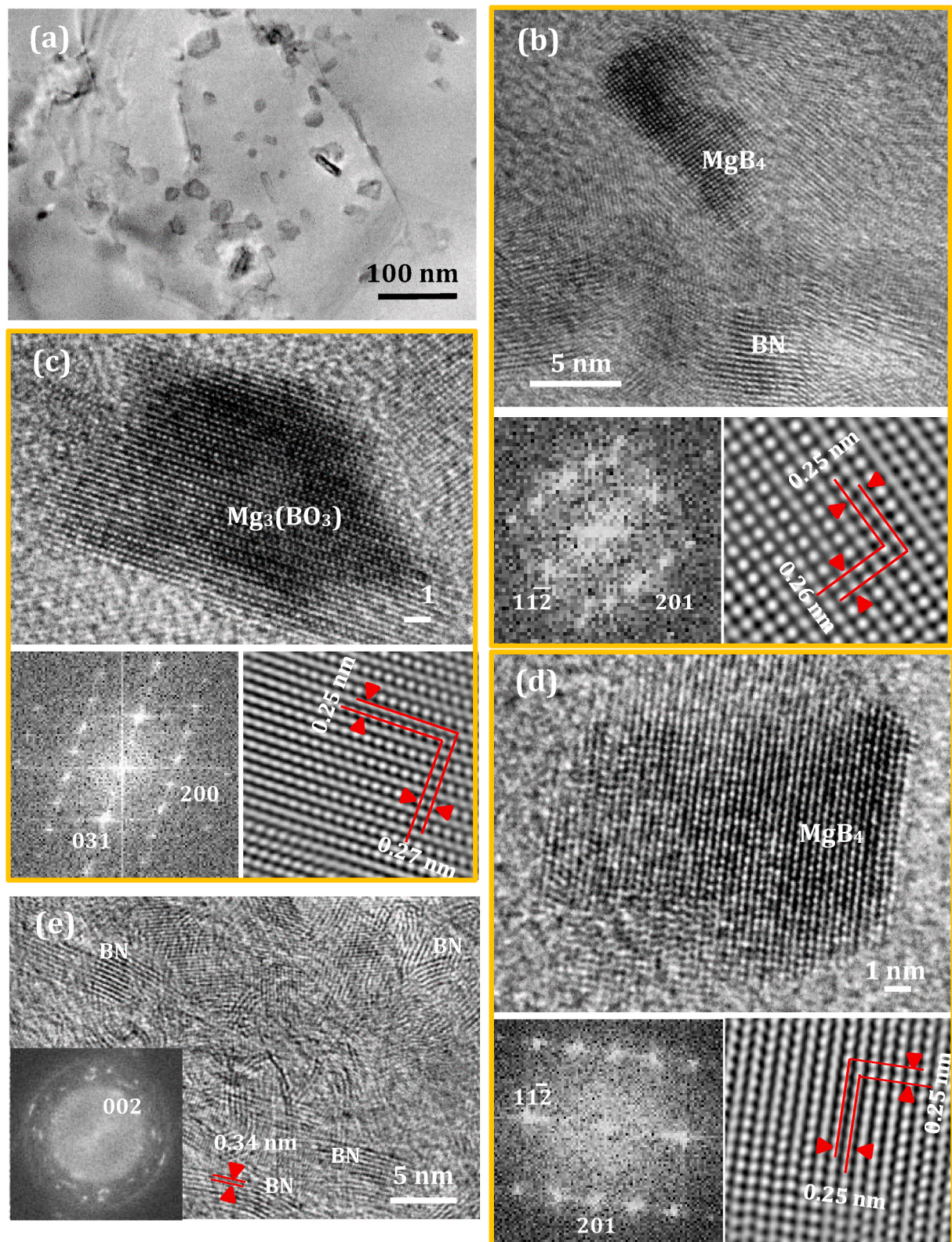


**Fig. 10.** TEM (a) and high-resolution TEM micrographs with corresponding FFT and IFFT images (b–e) showing the presence of  $\text{MgB}_2$  (b, d),  $\text{Mg}_3(\text{BO}_3)_2$  (c) and BN phases in Al7-BN composite.

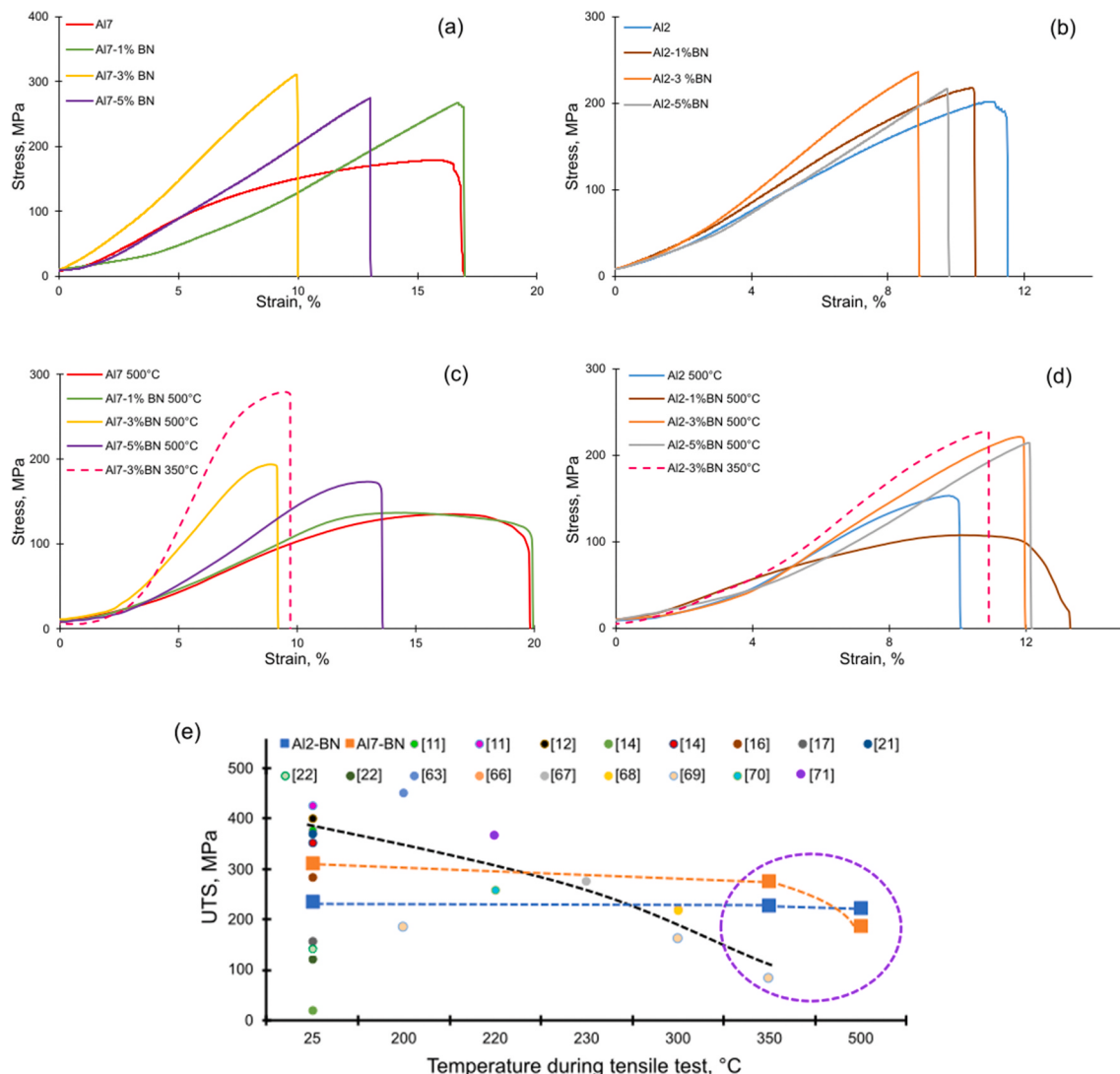


**Fig. 11.** Representative room-temperature (a,b) and elevated-temperature (c,d) stress-displacement curves of Al7 (a,c) and Al2 (b,d) samples with and without BN additives. Comparison of tensile strength values of Al-based composites at different temperatures (e). Dotted lines are only used as a guide to the eye.

#### 4.2. Mechanical properties and reinforcing mechanisms

Hardness of the Al7-BN composite (130 HV) was greater than that of stir-casted Al7075-12% $\text{B}_4\text{C}$ -3% $\text{MoS}_2$  (94 HV) [57] and Al7075-9% $\text{B}_4\text{C}$ -3%BN (100 HV) [58], as cast Al7075-2-3%SiC (90–98 HV) [59,60], and Al7075-6% $\text{Al}_2\text{O}_3$  (110 HV) [61]. The larger hardness was reported for as-cast Al7075-1.2% $\text{Al}_2\text{O}_3$  material [62].

Through using a combination of HEBM and SPS, we have successfully fabricated dense Al-BN composites with large hardness and high tensile strength at both room and high temperatures from the powder mixtures of individual elements. The tensile strength of the present Al2-3%BN and Al7-3%BN composites at 500 °C significantly exceeds that of any of the commercial Al alloys and Al-based composites fabricated so far. In addition, the Al2-3%BN sample demonstrated a decently high strength (>220 MPa) in a wide temperature range (25–500 °C). Although the tensile strength of Al7-3%BN at room temperature (310 MPa) was slightly lower compared with the best Al-BN composites, it was significantly higher at 500 °C (Table 1).

Al alloys and composites display strain-softening during heating. Available literature data on the mechanical properties of Al2- and Al7-based composites at elevated temperatures are rather scarce. The UTS values of Al2014-T6 and Al7075-T6 alloys rapidly decrease with increasing temperature from 480 (25 °C) to 30 MPa (370 °C) and from

570 (25 °C) to 40 MPa (370 °C), respectively. The tensile strength of other commercial as-cast Al2024, Al2219, and Al2618 materials is below 200 MPa already at 200 °C [63]. The mechanical properties of alumina strengthened Al-based composites also deteriorate rapidly with increasing temperature. For example, the tensile strength of  $\text{Al}_2\text{O}_3$  fiber-reinforced Zn-Al alloy composites decreased from 350 MPa (RT) to 100 MPa (200 °C) [64] and that of  $\text{Al}_2\text{O}_3/\text{Al-Zn-Mg-Cu}$  composite decreased from 210 MPa (220 °C) to 50 MPa (400 °C) [65]. Strength weakening at elevated temperatures limits their industrial applications. Increased strength (but at significantly lower temperatures) was reported for Al2009-1.5 vol%CNT composites (220 MPa at 300 °C) [66], nanostructured Al-Mg-Si alloys fabricated by severe plastic deformation (275 MPa at 230 °C) [67], as-cast Al-27%Cu-5%Si alloys (217 MPa at 300 °C) [68], Al-Ni-Zr composites (175–191 MPa (200 °C)), 155–166 (300 °C), and 82 MPa (350 °C) [69], nano-sized TiCp/Al-Cu (258 MPa at 220 °C) [70], ( $\text{TiB}_2$ -TiC)/Al-Cu-Mg-Si composites (366 MPa at 220 °C) [71], and Sc- and Mg-doped Al2219 alloys (450 MPa at 200 °C) [63]. Note, that various types of subsequent machining, such as extrusion [62, 72] or friction stir processing [59] can improve strength. The reinforcing particles, which are stable at elevated temperatures, were proposed to prevent grain boundary sliding and formation of microvoids.

The presence of different oxide, boride, and intermetallic inclusions increases the hardness and strength by precipitation strengthening

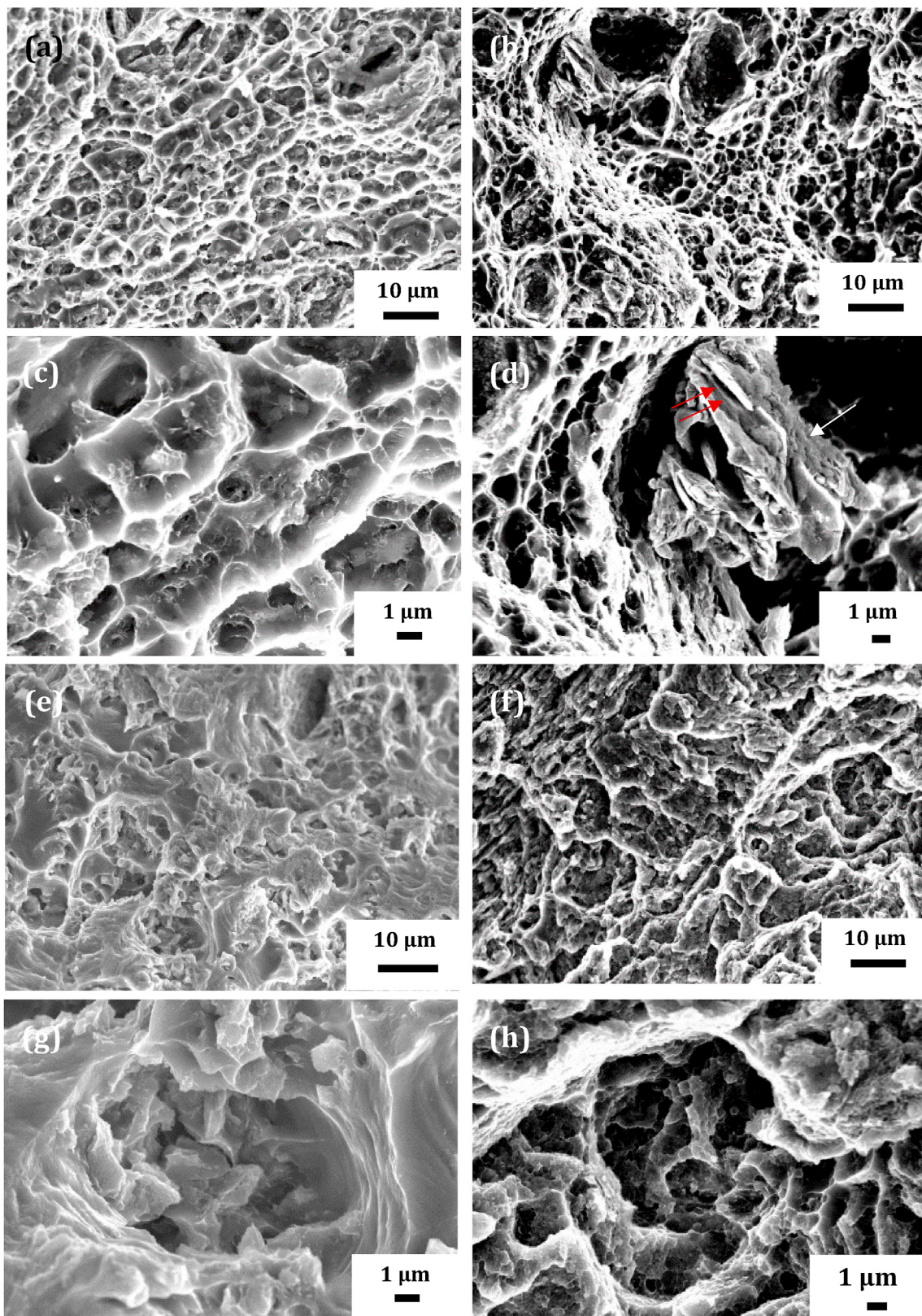


**Fig. 12.** SEM fracture micrographs of Al2 (a,c), Al2–3%BN (b,d), Al7 (e,g) and Al7–3%BN (f,h) samples after the tensile tests at room temperature.

mechanism. For example, the precipitation of hard  $MgB_2$  and  $Mg_3(BO_3)_2$  inclusions should contribute to the high material hardness. In addition, Cu, Fe, Mg, Mn, Si, and Zn dissolve in an Al-based matrix and increase the lattice distortion, which leads to an increase in the strength and hardness of the Al2- and Al7-based composites due to solid-solution

hardening. During SPS and subsequent cooling these elements also precipitate in the form of second phases contributing to the Orowan strengthening. The plate-like precipitates with sharp interfaces and those having a spherical/globular shape were located both inside the Al-based grains and at the grain boundaries. These nanoparticles are

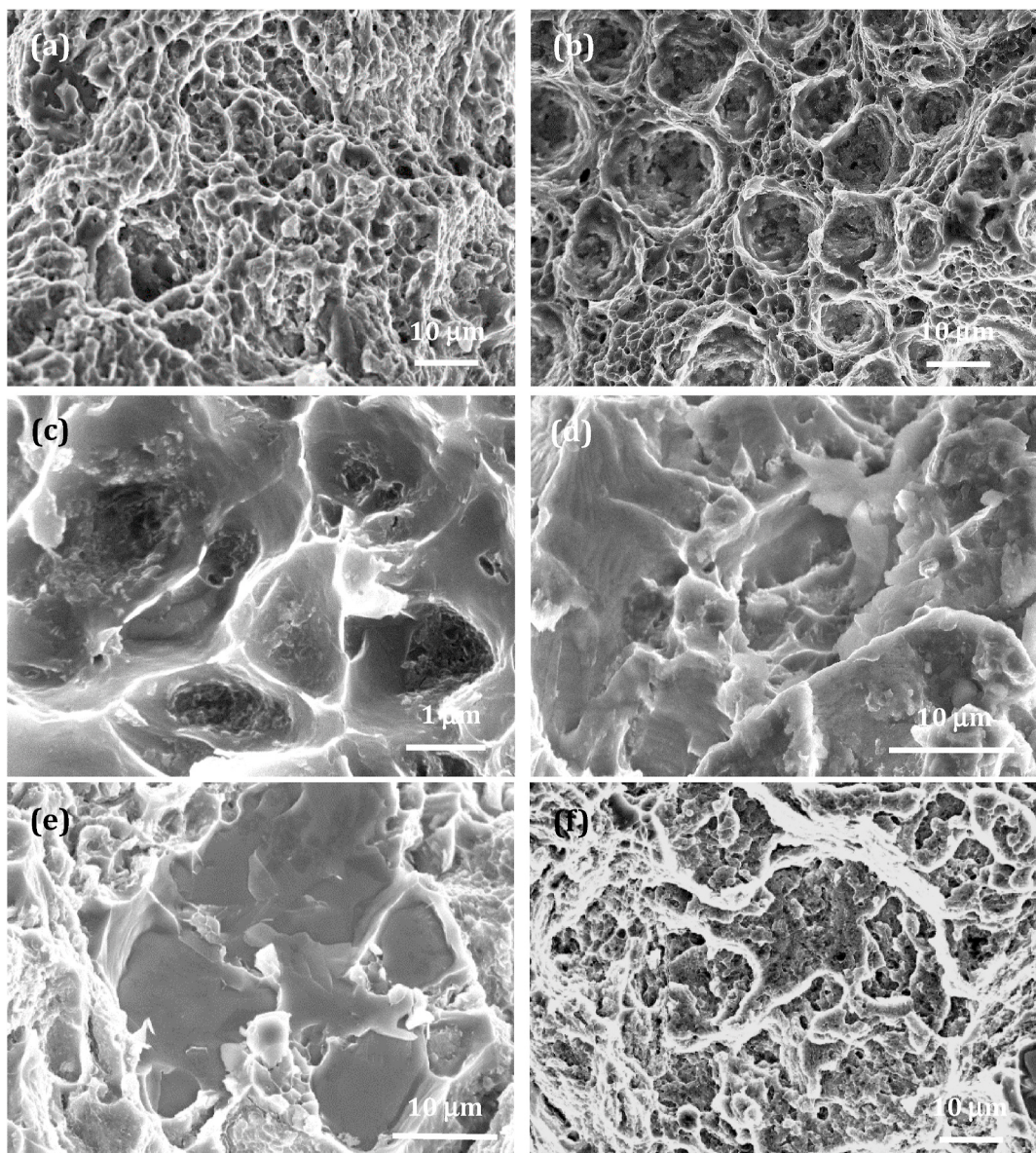


**Fig. 13.** SEM fracture micrographs of Al2 (a), Al2-3% BN (b,c), Al7 (d,e), and Al7-3%BN (f) samples after the tensile tests at 500 °C.

**Table 5**

Phase composition of the Al-based composite materials verified by different methods.

Sample	Phase composition		
	XRD	SEM/EDS	TEM
Al2	Al-based matrix, AlCu <sub>3</sub> , Al <sub>2</sub> Cu	Al(Mg,Si,Mn,Fe,Cu), AlCu <sub>x</sub> , MgO <sub>x</sub>	Al <sub>5</sub> Cu <sub>6</sub> Mg <sub>2</sub>
Al2-3% BN	Al-based matrix, AlCu <sub>3</sub>	Al(Mg,Si,Mn,Fe,Cu), AlCu <sub>x</sub> , AlB <sub>2</sub> , SiN <sub>x</sub>	Al <sub>5</sub> Cu <sub>6</sub> Mg <sub>2</sub> , Al <sub>6</sub> CuMg <sub>4</sub> , MgO <sub>2</sub>
Al7	Al-based matrix, AlCu <sub>3</sub> , Al <sub>2</sub> Cu, Al <sub>5</sub> Cu <sub>6</sub> Mg <sub>2</sub>	Al(Cu,Zn,Mg), AlCu <sub>x</sub> , Fe(Al,Cu), MgO <sub>x</sub>	AlCu <sub>3</sub> , Al <sub>2</sub> Cu/Fe <sub>3</sub> Al, Al <sub>5</sub> Cu <sub>6</sub> Mg <sub>2</sub> , Al <sub>4</sub> Cu <sub>9</sub> , MgO <sub>2</sub>
Al7-3% BN	Al-based matrix BN	Al(Cu,Zn,Mg), AlCu <sub>x</sub> , BN, BNO, MgB <sub>x</sub> , MgO <sub>x</sub> , MgN <sub>x</sub> O <sub>y</sub>	MgB <sub>2</sub> , Mg <sub>3</sub> (BO <sub>3</sub> ) <sub>2</sub> , BN

barriers for dislocation movement in an Al-based matrix.

Large particles can create local stress concentration and initiate crack nucleation [73]. The reinforcing particles in Al2-3%BN and Al7-3%BN composites have three characteristic dimensions: 5–30 nm, 60–220 nm, and 1–2 μm. Such a trimodal size distribution can be beneficial in terms of more homogeneous stress distribution. The enhanced mechanical properties can be also attributed to the various reinforced phases with nanoscale dimensions.

The enhanced mechanical properties of Al2-3%BN and Al7-3%BN composites at 500 °C can be attributed to their superior thermal stability. The Al-Cu intermetallic phases are characterized by high thermal stability; the Al<sub>2</sub>Cu ( $\theta$ ), AlCu ( $\eta'$ ), Al<sub>3</sub>Cu<sub>4</sub> ( $\zeta'$ ), and Al<sub>4</sub>Cu<sub>9</sub> ( $\delta$ - and  $\gamma'$ ) phases are stable below 580 °C [74]. Al alloys with the cubic  $\sigma$ -phase Al<sub>5</sub>Cu<sub>6</sub>Mg<sub>2</sub> are of particular interest for high-temperature applications due to their low coarsening rate [75]. The microstructures of Al2, Al2-3%BN, Al7, and Al7-3%BN composites after high-temperature tensile tests are illustrated in Fig. S10. No Al grain growth or

reinforcing nanoparticle coalescence are observed. The homogeneous nanoparticle distribution within the metallic matrix was fully preserved even after heating to 500 °C. The Al grain boundaries are completely decorated by thermally stable intermetallic compounds, which act as a diffusion barrier to Al atoms, preventing their rapid coarsening (Fig. S10c). Since the grain boundary sliding is the main deformation mechanism at elevated temperatures, nanoparticle segregation along the grain boundaries can increase their strength. The comparison of SEM micrographs presented in Fig. S10 also documents the microstructural differences between the BN-free and BN-incorporated samples. Without BN additives, most of the reinforcing particles segregate along the Al grain boundaries, while, in the case of Al-BN composites, they are more homogeneously distributed over the material volume (Figs. S10b and d).

#### 4.3. Role of h-BN flakes during ball milling process

##### 4.3.1. Theoretical insight

The important role of the BN additives in the microstructure formation (already at the ball milling stage) is discussed in more detail below. The SEM fracture micrographs show that in case of the Al-BN composites the fracture surface is more homogeneous due to a more uniform volume distribution of the reinforcing nanoparticles (Fig. S5). To reveal the lubricating contribution of BN additives during the ball milling process, the large-scale simulations of interaction between two Al nanoparticles with and without BN additives (Al/Al and Al/h-BN/Al interfaces) were carried out.

The developed model (based on MD simulations) describes the critical shear stress and its dependence on the pressure between nanoparticles. Critical shear stress is used in most models describing mechanical characteristics of composite materials [76]. The atomic structure of two types of interfaces (Al/Al and Al/h-BN/Al) is shown in Fig. 14. In the proposed model, Al polycrystalline grain contains five nanocrystallites with a 5 nm side size (shown by green color).

Upper Al nanoparticle is moved stepwise along the X axis (Fig. 14) with a step of 0.1 Å and for each position the total energy is calculated. Total displacement of the top nanoparticle is about 3 nm. Then the

maximum force along the path and the  $\tau_c$  parameter, defined as the maximum force divided by the interface area, was calculated. To avoid displacement of the whole system during the movement of the upper Al nanoparticle, the lowest atomic plane of bottom Al nanoparticle was fixed along X direction (shown by blue color in Fig. 14). For a more complete description of the nanoparticle interaction, it is necessary to take into account the force (pressure) with which the upper particle acts onto the lower one. To account for this in the model, the active plane was added to the system (shown by grey color) to create a mechanical stress. By changing the plane position, the pressure changes were modeled.

Simulations were carried out at a constant temperature of 100 K and pressures of 1.1 GPa and 5.2 GPa. Fig. 14c and d shows the dependence of shear force on nanoparticle displacement at a pressure of 1.1 GPa (c) and 5.2 GPa (d) for the Al/Al (black) and Al/h-BN/Al (red) interfaces. Results indicate that at a pressure of 1.1 GPa the force that must be applied to move the top Al nanoparticle relative to the bottom one is 40% higher for the Al/Al interface compared with the Al/h-BN/Al interface. When the applied pressure is increased from 1.1 to 5.2 GPa, the friction force between two Al nanoparticles slightly increases from 78 nN to 87 nN, whereas for the Al/h-BN/Al system it significantly increases from 45 nN to 65 nN. To explain the obtained results, a detailed analysis of changes in the atomic structure during Al nanoparticles displacement was carried out.

The atomic structures of Al/Al and Al/h-BN/Al interfaces at the start (0 nm) and end (3 nm) positions at pressures of 1.1 GPa and 5.2 GPa are demonstrated in Fig. 15. For better illustration of the nanoparticle displacement relative to each other, the specific atomic areas are highlighted in red (Fig. 15a and b). The presence of a h-BN monolayer significantly decreases friction between the two Al nanoparticles and their atomic structure remains unchanged (bottom panels in Fig. 15a and b). In the absence of the intermediate h-BN layer, the bottom atomic layer is subjected to sequential displacements (top panels in Fig. 15a and b). With increasing load, the friction force and displacement profile slightly change. In case of the Al/Al interface, the critical shear stress increases from 3.17 GPa to 3.57 GPa. It can be suggested that without

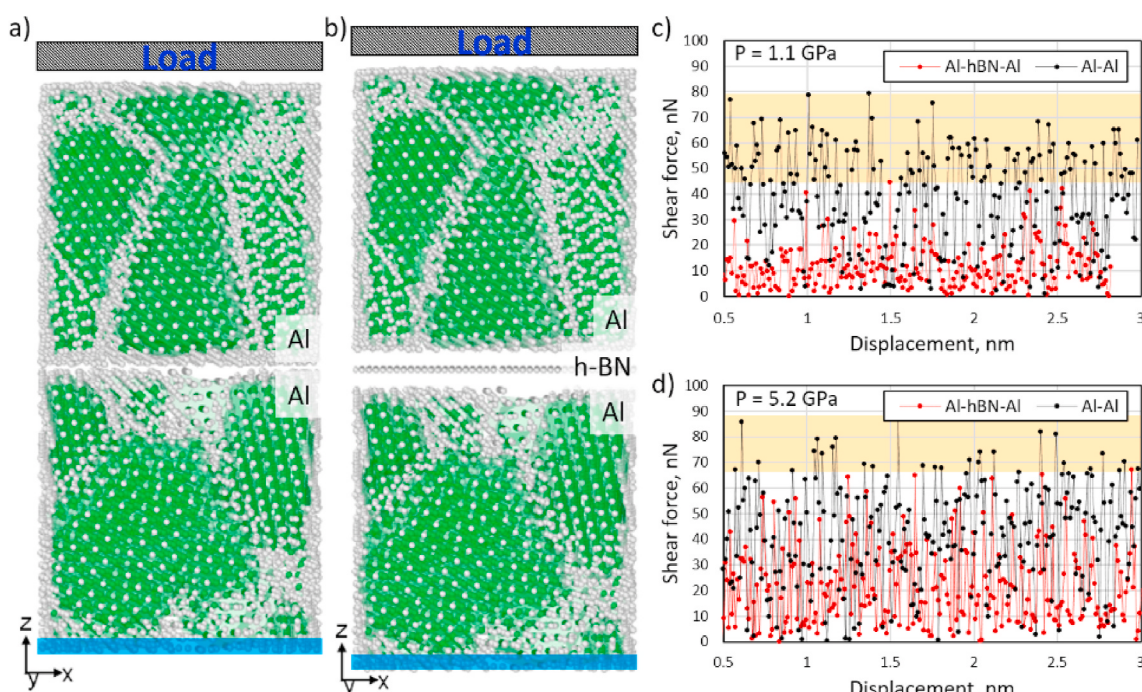


**Fig. 14.** Atomic structures of Al/Al (a) and Al/h-BN/Al interfaces (b). Each Al polycrystalline grain contains five nanocrystallites with 5 nm side size (shown by green color). The dependence of shear force on displacement at a pressure of 1.1 GPa (c) and 5.2 GPa (d). Black and red colors show dependencies for the Al/Al and Al/h-BN/Al interfaces, respectively. (For interpretation of the references to color in this figure legend, the reader is referred to the Web version of this article.)

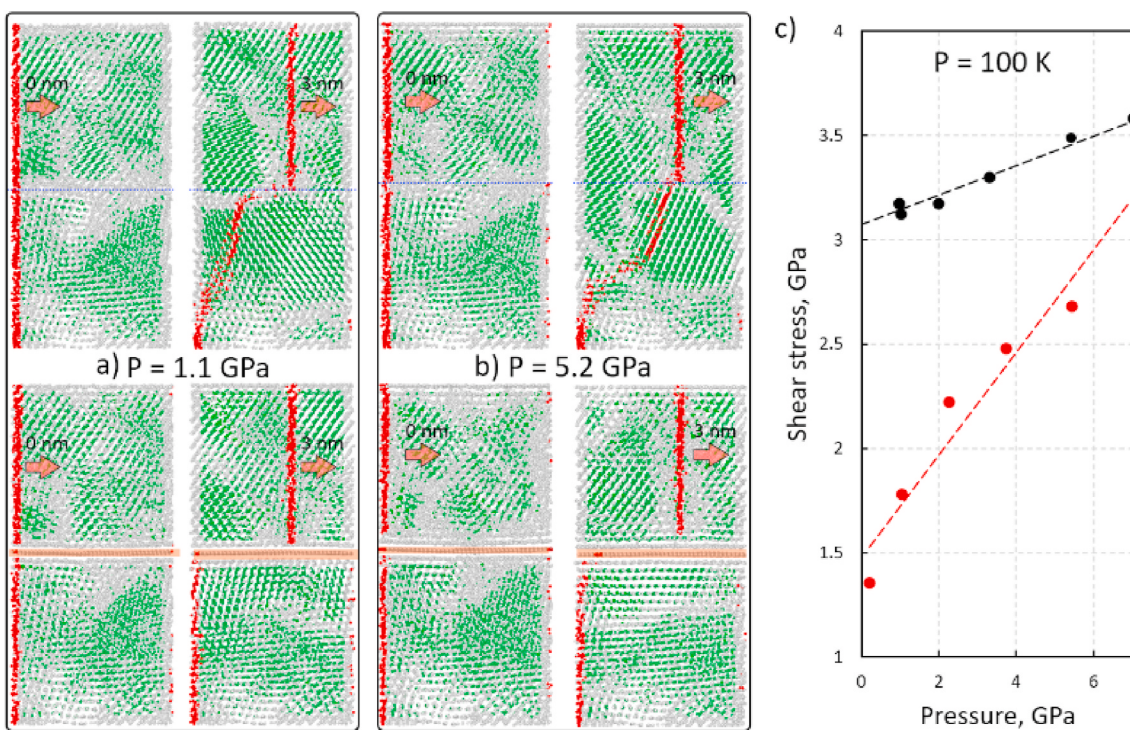


**Fig. 15.** Atomic structures of Al/Al (top panels) and Al/h-BN/Al (bottom panels) systems during Al nanoparticle displacements by a maximum distance of 3 nm at a pressure of 1.1 (a) and 5.2 GPa (b). Dashed blue lines (top panels) and thick orange lines (bottom panels) denote the Al/Al interface and the h-BN monolayer, respectively. The dependence of critical shear stress on pressure between Al nanoparticles with (red) and without (black) h-BN intermediate layer (c). (For interpretation of the references to color in this figure legend, the reader is referred to the Web version of this article.)

the h-BN layer two Al nanoparticles would agglomerate.

The presence of h-BN intermediate layer significantly changes the Al nanoparticle displacement mechanism. The top Al nanoparticle slides relative to the bottom one. An increase in pressure from 1.1 GPa to 5.2 GPa does not lead to a change in the nanoparticle atomic structure. Only slight displacement of the intermediate h-BN layer is observed indicating an increase in the interaction force at the interface. In this case, Al nanoparticle agglomeration is not expected. Thus, the intermediate h-BN layer acts as a solid lubricant preventing the formation of Al nanoparticle agglomerates during ball milling.

The dependence of critical shear stress on pressure for the Al/Al (black) and Al/h-BN/Al (red) interfaces is depicted in Fig. 15c. For both interface types, the linear dependence is observed. Small slope of Al/Al system suggests nanoparticle agglomeration during ball milling process. Fast shear stress increase with pressure (Al/h-BN/Al system) indicates the absence of agglomeration. Unlike Al/Al system, further increase (while having h-BN inclusions) will lead to the Al nanoparticle destruction and formation of smaller nanoparticles. Thus, the theoretical results highlight the important role of h-BN additives during ball milling: h-BN nanosheets promote the formation of smaller Al grains and prevent Al nanoparticle agglomeration. The obtained results are also relevant for other metal particles in a powder mixture.

#### 4.3.2. Experimental verification

To verify the results of theoretical modelling, the powder mixtures after HEBM processing were molded into acrylic resin, polished, etched, and finally observed in an optical microscope. Without the BN additives, the Al particle size varies from 5 to 15  $\mu\text{m}$  (Figs. S11a and c). In contrast to the spherical shape of Al particles in the initial powder mixtures, the Al particles after HEBM have irregular shape indicating their strong deformation. The Al particles are entirely surrounded by a second phase. Since the corresponding XRD patterns only show peaks from the individual elements (Fig. 1), it is reasonable to assume that thin layers along the Al grain boundaries mostly contain Cu (Al2) and Zn (Al7).

Considering that the initial particle size of Al powder was 3–15  $\mu\text{m}$  (Fig. S1a), it can be suggested that some particles have kept their size, whereas the others could agglomerate. In the BN-containing powder, the Al particles are much smaller, *i.e.* 3.5–6.6  $\mu\text{m}$  (Al2–3%BN) and 3.5–10  $\mu\text{m}$  (Al7–3%BN). Thus, the experimental data are in a full agreement with the theoretical results indicating that the BN additives not only prevent Al particle agglomeration, but also promote the Al nanoparticle destruction and formation of smaller particles. An interesting observation is the formation of a layered structure in which the Al grains line up in a certain direction (Figs. S11d and e). This indicates sliding of Al grains relative to each other under an applied load and further proves BN-assisted lubrication during HEBM. Grain refinement significantly affected the composite structures after SPS. While the Al grain size in the SPS-fabricated composites with and without BN phase was similar (Table 4), indicating no contribution of the Hall-Petch mechanism for the material strength, the reinforcing particles in the BN-containing composites were smaller and more homogeneously distributed over the composite volume. This can be explained by a shorter diffusion distance and more complete phase transformation at a relatively low temperature (below Al melting point) within more homogeneous fine powder mixture during SPS. Thus, adding h-BN phase provides solid lubrication, prevents nanoparticle agglomeration during HEBM and leads to more homogeneous phase distribution in the powder mixtures and the resultant composites.

## 5. Conclusions

Al2014 (Al2) and Al7075 (Al7) series composites loaded with 1, 3, and 5 wt% of h-BN platelets were successfully fabricated by using a combination of high energy ball milling and spark plasma sintering (SPS) from the powder mixtures of individual elements. The best set of mechanical properties was achieved for the composites reinforced with 3 wt% of BN. Compared to the h-BN-free materials the hardness increased by 34% (Al7–3%BN) and 62% (Al2–3%BN). The maximum

room-temperature tensile strength of 310 MPa was documented for the Al7–3%BN sample. By doping with 3 wt% of *h*-BN phase, the tensile strength was increased by 16% (25 °C) and 40% (500 °C) for Al2 series composites and by 74% (25 °C) and 40% (500 °C) for Al7 series samples. In the case of Al2–3%BN composite, the tensile strength values at 300 °C (227 MPa) and 500 °C (221 MPa) were only 4% and 6% lower than that at 25 °C (236 MPa). The superior mechanical properties were attributed to a combination of high thermal stability of reinforcing inclusions, solid solution hardening, and Orowan (precipitation) strengthening. The important role of the BN additives in the microstructure formation during the ball milling stage was clearly demonstrated using atomistic simulations. Results indicated that the *h*-BN nanosheets had prevented Al nanoparticle agglomeration, promoted their refinement, and led to more homogeneous phase distribution in the powder mixtures and the resultant composites. During SPS, the BN additives reacted with Al, Si, and Mg to form AlB<sub>2</sub>, SiN<sub>x</sub>, and MgB<sub>2</sub>/Mg<sub>3</sub>(BO<sub>3</sub>)<sub>2</sub> inclusions, which, together with unreacted *h*-BN nanoparticles contributed to the composites' strength.

## Data availability

The raw/processed data required to reproduce these findings cannot be shared at this time as the data also forms part of an ongoing study. Some data can be made available upon request.

## CRediT authorship contribution statement

**Shakti Corthay:** Conceptualization, Investigation, Writing – original draft. **Konstantin L. Firestein:** Investigation, Visualization. **Dmitry G. Kvashnin:** Simulation, Formal analysis. **Magzhan K. Kutzhanov:** Investigation, Visualization. **Andrei T. Matveev:** Investigation. **Andrey M. Kovalskii:** Investigation. **Denis V. Leybo:** Investigation. **Dmitri V. Golberg:** Writing – review & editing. **Dmitry V. Shtansky:** Formal analysis, Resources, Writing – review & editing, Supervision.

## Declaration of competing interest

The authors declare that they have no known competing financial interests or personal relationships that could have appeared to influence the work reported in this paper.

## Acknowledgements

The authors gratefully acknowledge the financial support from the Ministry of Education and Science of the Russian Federation (Increase Competitiveness Program of NUST “MISiS”, K2-2020-023). D.G. is grateful to the Australian Research Council (ARC) for granting a Laureate Fellowship No. FL160100089 and to the Central Analytical Research Facility (CARF) of QUT for granting an access to the high-resolution transmission electron microscope.

## Appendix A. Supplementary data

Supplementary data to this article can be found online at <https://doi.org/10.1016/j.msea.2021.140969>.

## References

- [1] G. Lutjering, J.C. Williams, Titanium, second ed., Springer-Verlag Berlin Heidelberg, 2007, p. 435, <https://doi.org/10.1007/978-3-540-73036-1>.
- [2] R. Haubner, M. Wilhelm, R. Weissenbacher, B. Lux, Boron nitrides - properties, synthesis and applications, in: High Performance Non-oxide Ceramics II, Springer-Verlag Berlin Heidelberg, 2002, pp. 1–45, [https://doi.org/10.1007/3-540-45623-6\\_1](https://doi.org/10.1007/3-540-45623-6_1).
- [3] Y. Xue, B. Jiang, L. Bourgeois, P. Dai, M. Mitome, C. Zhang, M. Yamaguchi, A. Matveev, C. Tang, Y. Bando, K. Tsuchiya, D. Golberg, Aluminum matrix composites reinforced with multi-walled boron nitride nanotubes fabricated by a high-pressure torsion technique, Mater. Des. 88 (2015) 451–460, <https://doi.org/10.1016/j.matdes.2015.08.162>.
- [4] M. Yamaguchi, F. Meng, K. Firestein, K. Tsuchiya, D. Golberg, Powder metallurgy routes toward aluminum boron nitride nanotube composites, their morphologies, structures and mechanical properties, Mater. Sci. Eng. A. 604 (2014) 9–17, <https://doi.org/10.1016/j.msea.2014.02.086>.
- [5] R. Gostariani, R. Ebrahimi, M.A. Asadabad, M.H. Paydar, Mechanical properties of Al/BN nanocomposites fabricated by planetary ball milling and conventional hot extrusion, Acta Metall. Sin. 31 (2018) 245–253, <https://doi.org/10.1007/s40195-017-0640-1>.
- [6] Y. Du, S. Li, K. Zhang, K. Lu, BN/Al composite formation by high-energy ball milling, Scripta Mater. 36 (1997) 7–14, [https://doi.org/10.1016/S1359-6462\(96\)00335-1](https://doi.org/10.1016/S1359-6462(96)00335-1).
- [7] K.L. Firestein, A.E. Steinman, I.S. Golovin, J. Cifre, E.A. Obraztsova, A.T. Matveev, A.M. Kovalskii, O.I. Lebedev, D.V. Shtansky, D. Golberg, Fabrication, characterization, and mechanical properties of spark plasma sintered Al-BN nanoparticle composites, Mater. Sci. Eng. A. 642 (2015) 104–112, <https://doi.org/10.1016/j.msea.2015.06.059>.
- [8] K.U. Yusupov, S. Corthay, A.V. Bondarev, A.M. Kovalskii, A.T. Matveev, D. Arkhipov, D.V. Golberg, D.V. Shtansky, Spark plasma sintered Al-based composites reinforced with BN nanosheets exfoliated under ball milling in ethylene glycol, Mater. Sci. Eng. A. 754 (2019) 74–81, <https://doi.org/10.1016/j.msea.2018.12.040>.
- [9] K.L. Firestein, S. Corthay, A.E. Steinman, A.T. Matveev, A.M. Kovalskii, I. V. Sukhorukova, D. Golberg, D.V. Shtansky, High-strength aluminum-based composites reinforced with BN, AlB<sub>2</sub> and AlN particles fabricated via reactive spark plasma sintering of Al-BN powder mixtures, Mater. Sci. Eng. A. 681 (2017) 1–9, <https://doi.org/10.1016/j.msea.2016.11.011>.
- [10] A.E. Steinman, S. Corthay, K.L. Firestein, D.G. Kvashnin, A.M. Kovalskii, A. T. Matveev, P.B. Sorokin, D.V. Golberg, D.V. Shtansky, Al-based composites reinforced with AlB<sub>2</sub>, AlN and BN phases: experimental and theoretical studies, Mater. Des. 141 (2018) 88–98, <https://doi.org/10.1016/j.matdes.2017.12.022>.
- [11] L.A. Dobrzański, A. Włodarczyk, M. Adamiāk, The structure and properties of PM composite materials based on EN AW-2124 aluminum alloy reinforced with the BN or Al<sub>2</sub>O<sub>3</sub> ceramic particles, J. Mater. Process. Technol. 175 (2006) 186–191, <https://doi.org/10.1016/j.jmatprotec.2005.04.031>.
- [12] H.R. Ezatpour, M. Torabi Parizi, S.A. Sajjadi, G.R. Ebrahimi, A. Chaichi, Microstructure, mechanical analysis and optimal selection of 7075 aluminum alloy based composite reinforced with alumina nanoparticles, Mater. Chem. Phys. 178 (2016) 119–127, <https://doi.org/10.1016/j.matchemphys.2016.04.078>.
- [13] R. Dasgupta, H. Meenai, SiC particulate dispersed composites of an Al-Zn-Mg-Cu alloy: property comparison with parent alloy, Mater. Char. 54 (2005) 438–445, <https://doi.org/10.1016/j.matchar.2005.01.012>.
- [14] N. Kaushik, P. Kumar, J. Ghose, S.K. Jha, Study of mechanical properties of Al2014-B4C-Gr hybrid nano composite, Mater. Today Proc. 33 (8) (2020) 5573–5576, <https://doi.org/10.1016/j.matpr.2020.03.560>.
- [15] L.A. Dobrzański, A. Włodarczyk-Fligier, M. Adamiāk, Composite materials based on EN AW-Al Cu4Mg1(A) aluminum alloy reinforced with the Ti(C,N) ceramic particles, Mater. Sci. Forum 530–531 (2006) 243–248, <https://doi.org/10.4028/www.scientific.net/MSF.530-531.243>.
- [16] V.V. Kumar, K. Raja, V.S. Chandra Sekar, T. Ramkumar, Thrust force evaluation and microstructure characterization of hybrid composites (Al7075/B<sub>4</sub>C/BN) processed by conventional casting technique, J. Brazilian Soc. Mech. Sci. Eng. 41 (2019) 228, <https://doi.org/10.1007/s40430-019-1728-5>.
- [17] P.B. Prakash, K.B. Raju, K. Venkatasubbaiah, N. Manikandan, Microstructure analysis and evaluation of mechanical properties of Al 7075 GNP's composites, Mater. Today Proc. 5 (2018) 14281–14291, <https://doi.org/10.1016/j.matpr.2018.03.010>.
- [18] M. Imran, A.R.A. Khan, S. Megeri, S. Sadik, Study of hardness and tensile strength of Aluminium-7075 percentage varying reinforced with graphite and bagasse-ash composites, Resour. Technol. 2 (2016) 81–88, <https://doi.org/10.1016/j.refit.2016.06.007>.
- [19] M.A. Jabbari Taleghani, E.M. Ruiz Navas, J.M. Torralba, Microstructural and mechanical characterisation of 7075 aluminium alloy consolidated from a premixed powder by cold compaction and hot extrusion, Mater. Des. 55 (2014) 674–682, <https://doi.org/10.1016/j.matdes.2013.10.028>.
- [20] S. Devaganesh, P.K. Dinesh Kumar, N. Venkatesh, R. Balaji, Study on the mechanical and tribological performances of hybrid SiC-Al7075 metal matrix composites, J. Mater. Res. Technol. 9 (2020) 3759–3766, <https://doi.org/10.1016/j.jmrt.2020.02.002>.
- [21] G.N. Ma, D. Wang, Z.Y. Liu, B.L. Xiao, Z.Y. Ma, An investigation on particle weakening in T6-treated SiC/Al-Zn-Mg-Cu composites, Mater. Char. 158 (2019) 109966, <https://doi.org/10.1016/j.matchar.2019.109966>.
- [22] P. Madhukar, N. Selvaraj, R. Gujjala, C.S.P. Rao, Production of high performance AA7150-1% SiC nanocomposite by novel fabrication process of ultrasonication assisted stir casting, Ultrason. Sonochem. 58 (2019) 104665, <https://doi.org/10.1016/j.ulsonch.2019.104665>.
- [23] A. Muthuchamy, A.R. Annamalai, S.G. Acharyya, N. Nagaraju, D.K. Agrawal, Microstructural and electrochemical behaviour of aluminium alloy composites produced using different sintering techniques, Mater. Res. 21 (2018), e20170321, <https://doi.org/10.1590/1980-5373-MR-2017-0321>.
- [24] A. EldeSouky, M. Johnsson, H. Svengren, M.M. Attallah, H.G. Salem, Effect of grain size reduction of AA2124 aluminum alloy powder compacted by spark plasma sintering, J. Alloys Compd. 609 (2014) 215–221, <https://doi.org/10.1016/j.jallcom.2014.04.136>.

- [25] J. Cheng, Q. Cai, B. Zhao, S. Yang, F. Chen, B. Li, Microstructure and mechanical properties of nanocrystalline Al-Zn-Mg-Cu alloy prepared by mechanical alloying and spark plasma sintering, *Materials* 12 (2019) 1255, <https://doi.org/10.3390/ma12081255>.
- [26] O. Molnárová, P. Málek, J. Veselý, P. Minárik, F. Lukáč, T. Chráska, P. Novák, F. Průša, The influence of milling and spark plasma sintering on the microstructure and properties of the Al7075 alloy, *Materials* 11 (2018) 547, <https://doi.org/10.3390/ma11040547>.
- [27] H. Queudet, S. Lemonnier, E. Barraud, J. Guyon, J. Ghanbaja, N. Allain, E. Gaffet, One-step consolidation and precipitation hardening of an ultrafine-grained Al-Zn-Mg alloy powder by Spark Plasma Sintering, *Mater. Sci. Eng. A* 685 (2017) 227–234, <https://doi.org/10.1016/j.msea.2017.01.009>.
- [28] H.-b. Chen, K. Tao, B. Yang, J.-S. Zhang, Nanostructured Al-Zn-Mg-Cu alloy synthesized by cryomilling and spark plasma sintering, *Trans. Nonferrous Metals Soc. China* 19 (2009) 1110–1115, [https://doi.org/10.1016/S1003-6326\(08\)60415-X](https://doi.org/10.1016/S1003-6326(08)60415-X).
- [29] F. Campbell, Elements of metallurgy and engineering alloys, *ASM Int.* (2008) 656, <https://doi.org/10.1361/emea2008p243>.
- [30] F. Czerwinski, Thermal stability of aluminum alloys, *Materials* 13 (2020) 3441, <https://doi.org/10.3390/ma13153441>.
- [31] ISO 6507 or GOST R ISO 6507-1, *Metals and Alloys. Vickers Hardness Test*, International Organization for Standardization, 2007.
- [32] ISO 3369, *Impermeable Sintered Metal Materials and Hard Metals Determination of Density*, 2006.
- [33] M.S. Daw, M.J. Baskes, Embedded-atom method: derivation and application to impurities, surfaces, and other defects in metals, *Phys. Rev. B* 29 (1984) 6443–6453, <https://doi.org/10.1103/PhysRevB.29.6443>.
- [34] X.W. Zhou, H.N.G. Wadley, R.A. Johnson, D.J. Larson, N. Tabat, A. Cerezo, A. K. Petford-Long, G.D.W. Smith, P.H. Clifton, R.L. Martens, T.F. Kelly, Atomic scale structure of sputtered metal multilayers, *Acta Mater.* 49 (2001) 4005–4015, [https://doi.org/10.1016/S1359-6454\(01\)00287-7](https://doi.org/10.1016/S1359-6454(01)00287-7).
- [35] A. Kinaci, J.B. Haskins, C. Sevik, T. Çağın, Thermal conductivity of BN-C nanostructures, *Phys. Rev. B* 86 (2012) 115410, <https://doi.org/10.1103/PhysRevB.86.115410>.
- [36] A.V. Krashenninnikov, N. Berseneva, D.G. Kvashnin, J. Enkovaara, T. Björkman, P. Sorokin, D. Shtansky, R.M. Nieminen, D. Golberg, Toward stronger Al-BN nanotube composite materials: insights into bonding at the Al/BN interface from first-principles calculations, *J. Phys. Chem. C* 118 (2018) 26894–26901, <https://doi.org/10.1073/pnas.1997-308X-2018-4-62-72>.
- [37] T. Björkman, Van der Waals density functional for solids, *Phys. Rev. B* 86 (2012) 165109, <https://doi.org/10.1103/PhysRevB.86.165109>.
- [38] S. Plimpton, Fast parallel algorithms for short-range molecular dynamics, *J. Comput. Phys.* 117 (1995) 1–19, <https://doi.org/10.1006/jcph.1995.1039>.
- [39] D. Broek, The role of inclusions in ductile fracture and fracture toughness, *Eng. Fract. Mech.* 5 (1973) 55–56, [https://doi.org/10.1016/0013-7944\(73\)90007-6](https://doi.org/10.1016/0013-7944(73)90007-6).
- [40] P. Villars, Al-Cu binary phase diagram 0.2–7 at.% Cu, [https://materials.springer.com/isp/phase-diagram/docs/c\\_0102006](https://materials.springer.com/isp/phase-diagram/docs/c_0102006).
- [41] Villars, P. Al-Zn binary phase diagram 0–45 at.% Zn, [https://materials.springer.com/isp/phase-diagram/docs/c\\_0906809](https://materials.springer.com/isp/phase-diagram/docs/c_0906809).
- [42] The Mg-Al binary phase diagram: datasheet from MSI Eureka in Springer Materials, [https://materials.springer.com/msi/phase-diagram/docs/sm\\_msi\\_r\\_10\\_012175\\_01\\_full\\_LnkDia0](https://materials.springer.com/msi/phase-diagram/docs/sm_msi_r_10_012175_01_full_LnkDia0).
- [43] O. Zobac, A. Kroupa, A. Zemanova, K.W. Richter, Experimental description of the Al-Cu binary phase diagram, *Metall. Mater. Trans. A* 50 (2019) 3805–3815, <https://doi.org/10.1007/s11661-019-05286-x>.
- [44] T. Soma, M. Ishizuka, H.M. Kagaya, Formation of AlCu solid solution and bulk properties, *Solid State Commun.* 95 (1995) 479–482, [https://doi.org/10.1016/0038-1098\(95\)00233-2](https://doi.org/10.1016/0038-1098(95)00233-2).
- [45] M. Draissia, M.Y. Debili, Study of solid-solution hardening in binary aluminium-based alloys, *Cent. Eur. J. Phys.* 3 (2005) 395–408, <https://doi.org/10.2478/bf02475646>.
- [46] G.F.V. Voort, J. Asensio-Lozano, The Al-Si phase diagram, *Microsc. Microanal.* 15 (2009) 60–61, <https://doi.org/10.1017/S1431927609092642>.
- [47] H. Mii, M. Senoo, I. Fujishiro, Solid solubility of Si in Al under high pressure, *Jpn. J. Appl. Phys.* 15 (1976) 777, <https://doi.org/10.1143/JJAP.15.777>.
- [48] J.B. Fogagnolo, D. Amador, E.M. Ruiz-Navas, J.M. Torralba, Solid solution in Al-4.5 wt% Cu produced by mechanical alloying, *Mater. Sci. Eng. A* 433 (2006) 45–49, <https://doi.org/10.1016/j.msea.2006.07.005>.
- [49] Y. Wei, J. Li, J. Xiong, F. Zhang, Investigation of interdiffusion and intermetallic compounds in Al-Cu joint produced by continuous drive friction welding, *Eng. Sci. Technol.* 19 (2016) 90–95, <https://doi.org/10.1016/j.jestch.2015.05.009>.
- [50] W.-W. Zhang, Y.-L. Zhao, D.-T. Zhang, Z.-Q. Luo, C. Yang, Y.-Y. Li, Effect of Si addition and applied pressure on microstructure and tensile properties of as-cast Al-5.0Cu-0.6Mn-1.2Fe alloys, *Trans. Nonferrous Metals Soc. China* 28 (2018) 1061–1072, [https://doi.org/10.1016/S1003-6326\(18\)64765-X](https://doi.org/10.1016/S1003-6326(18)64765-X).
- [51] J.E. Hatch, *Aluminum: Properties and Physical Metallurgy*, ASM International, American Society for Metals, 1984, p. 424.
- [52] A.E. Ares, S.F. Guejman, C.E. Schvezov, An experimental investigation of the columnar-to-equiaxed grain transition in aluminum-copper hypoeutectic and eutectic alloys, *J. Cryst. Growth* 312 (2010) 2154–2170, <https://doi.org/10.1016/j.jcrysgro.2010.04.040>.
- [53] W. Du, C. Song, F. Zhang, M. Jiang, Q. Zhai, K. Han, The effect of convection on microstructures and interface stability of Al-4.5wtPctCu alloy made by directional solidification, *Met. Mater. Trans. B* 46 (2015) 2423–2429, <https://doi.org/10.1007/s11663-015-0433-8>.
- [54] X. Liao, Q. Zhai, C. Song, W. Chen, Y. Gong, Effects of electric current pulse on stability of solid/liquid interface of Al-4.5 wt.% Cu alloy during directional solidification, *Mater. Sci. Eng. A* 466 (2007) 56–60, <https://doi.org/10.1016/j.msea.2007.02.022>.
- [55] X.B. Yang, J.H. Chen, J.Z. Liu, F. Qin, J. Xie, C.L. Wu, A high-strength AlZnMg alloy hardened by the T-phase precipitates, *J. Alloys Compd.* 610 (2014) 69–73, <https://doi.org/10.1016/j.jallcom.2014.04.185>.
- [56] J.Z. Liu, J.H. Chen, X.B. Yang, S. Ren, C.L. Wu, H.Y. Xu, J. Zou, Revisiting the precipitation sequence in Al-Zn-Mg-based alloys by high-resolution transmission electron microscopy, *Scripta Mater.* 63 (2010) 1061–1064, <https://doi.org/10.1016/j.scriptamat.2010.08.001>.
- [57] S. Liu, Y. Wang, T. Muthuramalingam, G. Anbuczezhiyan, Effect of B<sub>4</sub>C and MoS<sub>2</sub> reinforcement on micro-structure and wear properties of aluminum hybrid composite for automotive applications, *Composites Part B* 176 (2019) 107329, <https://doi.org/10.1016/j.compositesb.2019.107329>.
- [58] N. Ramadoss, K. Pazhanivel, G. Anbuczezhiyan, Synthesis of B<sub>4</sub>C and BN reinforced Al7075 hybrid composites using stir-casting method, *J. Mater. Res. Technol.* 9 (2020) 6297–6304, <https://doi.org/10.1016/j.jmrt.2020.03.043>.
- [59] A. Kumar, K. Pal, S. Mula, Effects of cryo-FSP on metallurgical and mechanical properties of stir cast Al7075-SiC nanocomposites, *J. Alloys Compd.* 852 (2021) 156295, <https://doi.org/10.1016/j.jallcom.2020.156925>.
- [60] A. Kumar, K. Pal, S. Mula, Simultaneous improvement of mechanical strength, ductility and corrosion resistance of stir cast Al7075-2%SiC micro- and nanocomposites by friction stir processing, *J. Manuf. Process.* 30 (2017) 1–13, <https://doi.org/10.1016/j.jmapro.2017.09.005>.
- [61] G.B.V. Kumar, C.S.P. Rao, N. Selvaraj, M.S. Bhagyashekar, Studies on Al 6061-SiC and Al 7075-Al<sub>2</sub>O<sub>3</sub> metal matrix composites, *J. Miner. Mater. Char. Eng.* 9 (2010) 43–55, <https://doi.org/10.4236/jmmce.2010.91004>.
- [62] H.R. Ezatpour, M. Torabi Parizi, S.A. Sajjadi, G.R. Ebrahimi, A. Chaichi, Microstructure, mechanical analysis and optimal selection of 7075 aluminum alloy based composite reinforced with alumina nanoparticles, *Mater. Chem. Phys.* 178 (2016) 119–127, <https://doi.org/10.1016/j.matchemphys.2016.04.078>.
- [63] S. Mondol, T. Alam, R. Banerjee, S. Kumar, K. Chattopadhyay, Development of a high temperature high strength Al alloy by addition of small amounts of Sc and Mg to 2219 alloy, *Mater. Sci. Eng. A* 687 (2017) 221–231, <https://doi.org/10.1016/j.msea.2017.01.037>.
- [64] S. Yu, W. Li, Z. He, Study on tensile strengths of Al<sub>2</sub>O<sub>3</sub> short fiber reinforced Zn-Al alloy composites at elevated temperatures, *JAC (J. Antimicrob. Chemother.)* 431 (2007) L8–L11, <https://doi.org/10.1016/j.jallcom.2006.05.094>.
- [65] Y.-L. Wu, C.-G. Chao, Deformation and fracture of Al<sub>2</sub>O<sub>3</sub>/Al – Zn – Mg – Cu metal matrix composites at room and elevated temperatures, *Mater. Sci. Eng. A* 282 (2000) 193–202, [https://doi.org/10.1016/S0921-5093\(99\)00762-5](https://doi.org/10.1016/S0921-5093(99)00762-5).
- [66] Z.Y. Liu, B.L. Xiao, W.G. Wang, Z.Y. Ma, Elevated temperature tensile properties and thermal expansion of CNT/2009Al composites, *Compos. Sci. Technol.* 72 (2012) 1826–1833, <https://doi.org/10.1016/j.compscitech.2012.07.021>.
- [67] R. Valiev, M.Yu Murashkin, I. Sabirov, A nanostructural design to produce high-strength Al alloys with enhanced electrical conductivity, *Scripta Mater.* 76 (2014) 13–16, <https://doi.org/10.1016/j.scriptamat.2013.12.002>.
- [68] S.A. Awe, Elevated temperature tensile properties of a ternary eutectic Al-27%Cu-5%Si cast alloy, *Int. J. Lightweight Mater. Manufact.* 4 (2021) 18–26, <https://doi.org/10.1016/j.jilmm.2020.07.004>.
- [69] L. Pan, S. Zhang, Y. Yang, N. Gupta, C. Yang, Y. Zhao, Z. Hu, High-temperature mechanical properties of aluminum alloy matrix composites reinforced with Zr and Ni trialuminides synthesized by in situ reaction, *Metall. Mater. Trans. A* 51 (2019) 214–225, <https://doi.org/10.1007/s11661-019-05511-7>.
- [70] W.-S. Tian, Q.-L. Zhao, Q.-Q. Zhang, F. Qiu, Q.-C. Jiang, Simultaneously increasing the high-temperature tensile strength and ductility of nano-sized TiCp reinforced Al-Cu matrix composites, *Mater. Sci. Eng. A* 717 (2018) 105–112, <https://doi.org/10.1016/j.msea.2018.01.069>.
- [71] Y.-Y. Gao, F. Qiu, Q.-L. Zhao, Q.-C. Jiang, A new approach for improving the elevated-temperature strength and ductility of Al-Cu-Mg-Si alloys with minor amounts of dual-phased submicron/nanosized TiB<sub>2</sub>-TiC particles, *Mater. Sci. Eng. A* 764 (2019) 138266, <https://doi.org/10.1016/j.msea.2019.138266>.
- [72] B. Chen, X.Y. Zhou, B. Zhang, K. Kondoh, J.S. Li, M. Qian, Microstructure, tensile properties and deformation behaviors of aluminum metal matrix composites co-reinforced by ex-situ carbon nanotubes and in-situ alumina nanoparticles, *Mater. Sci. Eng. A* 795 (2020) 139930, <https://doi.org/10.1016/j.msea.2020.139930>.
- [73] M.S. Xie, Z. Wang, G.Q. Zhang, C. Yang, W.W. Zhang, K.G. Prashanth, Microstructure and mechanical property of bimodal-size metallic glass particle-reinforced Al alloy matrix composites, *J. Alloys Compd.* 814 (2020) 152317, <https://doi.org/10.1016/j.jallcom.2019.152317>.
- [74] O. Zobac, A. Kroupa, A. Zemanova, K.W. Richter, Experimental description of the Al-Cu binary phase diagram, *Metall. Mater. Trans. A* 50 (2019) 3805–3815, <https://doi.org/10.1007/s11661-019-05286-x>.
- [75] Q. Li, F.E. Wawner, Characterization of a cubic phase in an Al-Cu-Mg-Ag alloy, *J. Mater. Sci.* 32 (1997) 5363–5370, <https://doi.org/10.1023/A:1018675029786>.
- [76] S.R. Bakshi, D. Lahiri, A. Agarwal, Carbon nanotube reinforced metal matrix composites - a review, *Int. Mater. Rev.* 55 (2010) 41–64, <https://doi.org/10.1179/09566009X1257253017053>.